Modelling low-frequency volcanic earthquakes in a viscoelastic medium with topography

Philippe Jousset,[1,*] Jürgen Neuberg[2] and Arthur Jolly[3,†]

[1] *BRGM, 3 Avenue Claude Guillemin, PO Box 6009, 45060 Orleans Cedex 02, France. E-mail: p.jousset@brgm.fr*
[2] *School of Earth Sciences, University of Leeds, Leeds LS2 9JT, UK. E-mail: locko@earth.leeds.ac.uk*
[3] *Geology Department, University of Hawaii, 200W. Kawili Street, Hilo, HI, 96720, USA. E-mail: ajolly@hawaii.edu*

SUMMARY

Magma properties are fundamental to explain the volcanic eruption style as well as the generation and propagation of seismic waves. This study focusses on magma properties and rheology and their impact on low-frequency volcanic earthquakes. We investigate the effects of anelasticity and topography on the amplitudes and spectra of synthetic low-frequency earthquakes. Using a 2-D finite-difference scheme, we model the propagation of seismic energy initiated in a fluid-filled conduit embedded in a homogeneous viscoelastic medium with topography. We model intrinsic attenuation by linear viscoelastic theory and we show that volcanic media can be approximated by a standard linear solid (SLS) for seismic frequencies above 2 Hz. Results demonstrate that attenuation modifies both amplitudes and dispersive characteristics of low-frequency earthquakes. Low frequency volcanic earthquakes are dispersive by nature; however, if attenuation is introduced, their dispersion characteristics will be altered. The topography modifies the amplitudes, depending on the position of the seismographs at the surface. This study shows that we need to take into account attenuation and topography to interpret correctly observed low-frequency volcanic earthquakes. It also suggests that the rheological properties of magmas may be constrained by the analysis of low-frequency seismograms.

Key words: dispersion, finite difference, low-frequency volcanic earthquakes, topography, viscoelasticity, wave equation.

1 INTRODUCTION

Magma properties are fundamental to the explanation of the volcanic eruption style as well as the generation and propagation of seismic waves. This study focuses on magma properties and rheology and their impact on low-frequency volcanic earthquakes. The aim of this study is to constrain magma properties and rheology by investigating their impact on low-frequency volcanic earthquakes.

The eruptive behaviour is dependent on many parameters, amongst which the rheology of the magma plays an important role (Dingwell & Webb 1989; Barmin *et al.* 2002). In particular, the transition in the properties of the melt phase from a liquid-like to a solid-like response in a cooling magma (glass transition) is one of the most fundamental phenomena that influences the eruptive style of volcanic rocks (Dingwell & Webb 1989; Stevenson *et al.* 1995). Similar to many volcanoes around the world, Soufrière Hills volcano, Montserrat, presents a variety of eruption styles ranging from dome grows and collapses (Young *et al.* 1998) to Vulcanian explosions.

The observation and modelling of seismic waves is one of several different ways to study volcanoes, aiming at a better understanding of volcanic processes. Long-period earthquakes and tremor are important waveforms in volcano seismology (Chouet 1996a), as they have been observed at many active volcanoes: e.g., Arenal, Costa Rica (Hagerty *et al.* 2000); Erebus, Antartica (Rowe *et al.* 2000); Galeras, Colombia (Gil Cruz & Chouet 1997; Gómez & Torres 1997); Karymsky, Russia (Johnson & Lees 2000); Mount St Helens, USA (Fehler & Chouet 1982); Lascar, Chile (Hellweg 2000); Redoubt, Alaska (Power *et al.* 1994; Chouet *et al.* 1994); Soufrière Hills, Montserrat (Aspinall *et al.* 1998; Miller *et al.* 1998; Neuberg *et al.* 1998; White *et al.* 1998). At Montserrat, a continuum exists between long-period and hybrid events, the latter having an additional high-frequency content (Neuberg *et al.* 2000). Throughout the paper, we refer to both types as low-frequency earthquakes (Jousset *et al.* 2003). Low-frequency earthquakes, whose frequency content ranges from 0.2 to 5 Hz, last several tens of seconds

*Formerly at: School of Earth Sciences, University of Leeds, Leeds LS2 9JT, UK.
†Formerly at: Montserrat Volcano Observatory, Flemming's, Montserrat, West Indies.
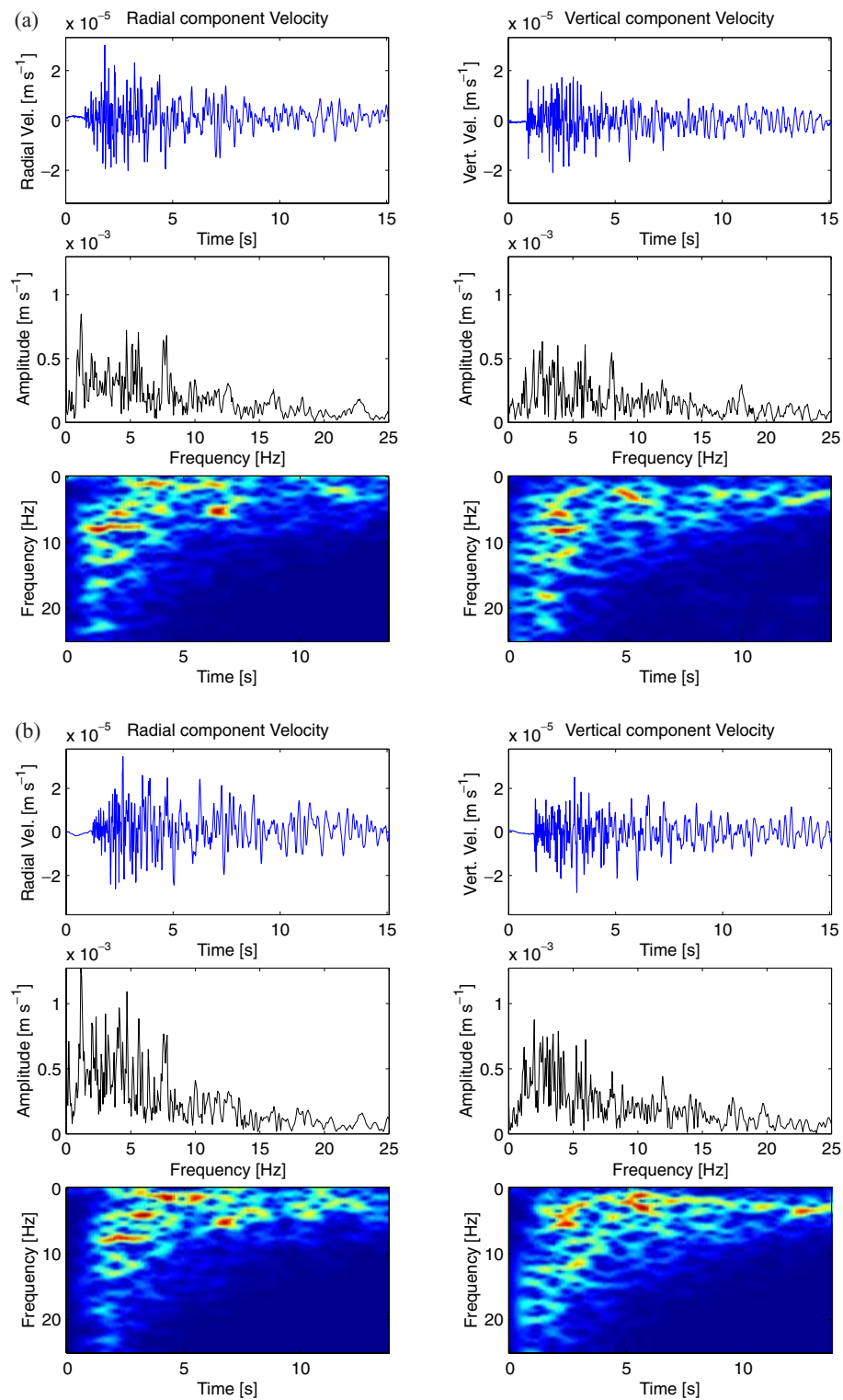
Figure 1. Two examples of long-period earthquakes from Montserrat volcano recorded on the 1999 July 7 at (a) 22:28 h and (b) 23:15 h UT at the three-component station MBBY (Güralp 40-T broad-band seismometer located 16°41′7N, 62°12′15E). Horizontal components were rotated in their radial and tangential components, with respect to the dome. Spectra and spectrograms are displayed for the radial and vertical components only, for a better comparison with our 2-D synthetic seismograms. We computed the spectrograms using a 0.8-s time window. Note that these events are very similar, suggesting that a non-destructive source process produces them.

(e.g. Fig. 1) and often occur in swarms of multiplets. Their characteristics are very similar both in time and frequency domain, suggesting that the processes generating these events are the same.

In recent years, good progress has been made in the understanding of the generation of the associated wavefield. Most models rely on the excitation of normal modes in fluid–solid systems (Biot 1952; Kubotera 1974; Chouet 1985, 1986; Ferrazzini & Aki 1987; Chouet 1988, 1992).

Neuberg *et al.* (1998) and Neuberg & O'Gorman (2002) propose a model where a source of seismic waves is triggered inside the volcanic conduit filled with a gas–melt mixture with depth-dependent properties. The resulting synthetic wavefield matches well the characteristics of observed low-frequency events at Montserrat. The seismic energy that forms a resonance by propagating as interface waves up and down the conduit boundaries, is released at the ends of the conduit at regular time intervals, interacts with the free-surface and travels as surface waves along the topography to the seismic stations (Jousset *et al.* 2003). Using realistic magma properties (Sturton & Neuberg 2003), this model explains also the frequency properties of those earthquakes in swarms: their time dependence is observed as gliding spectral lines (Jousset *et al.* 2003).

An interesting feature of low-frequency earthquakes is that they display dispersion characteristics including both normal and inverse dispersion (Chouet 1986; Ferrazzini & Aki 1987), which has been successfully modelled in previous studies (Neuberg 2000; Jousset *et al.* 2003). However, wave dispersion may also be a result of wave propagation in anelastic media (Carcione *et al.* 1988). The volcanic conduit is filled with a hot, viscous, multiphase medium and the volcano edifice is made of heterogeneous materials. Consequently, both amplitudes and dispersion characteristics of seismic waves are affected by anelastic volcanic media (Kumagai & Chouet 1999, 2000a,b; Kumagai *et al.* 2002a). One objective of this study is to determine the impact that internal friction of volcanic media (both in the conduit as intrinsic dissipation and in the solid as anelastic attenuation) has on properties of low-frequency earthquakes in time and frequency. Scattering of seismic waves has also been shown to be a way to attenuate seismic energy (Hellweg 2003; Wegler 2003). However, intrinsic attenuation contributes significantly higher to attenuation compared with scattering (Gudmundsson *et al.* 2004). Therefore, we do not address wave scattering in this study.

Low-frequency earthquakes on Montserrat are observed as surface waves, which display complex elliptical particle motions at the free surface (Miller *et al.* 1998). Ohminato & Chouet (1997) and Neuberg & Pointer (2000) pointed out the importance of the topography on particle motions and wave forms. Moreover, topography affects the seismic amplitudes and must be taken into account if the effects of other parameters on amplitudes, like attenuation, are to be investigated. Therefore, we present in this work a formulation for the computation of the wave propagation allowing for topography.

Numerical models of low-frequency earthquakes to date (Chouet 1986; Neuberg 2000; Jousset *et al.* 2003) do not commit themselves on the actual trigger mechanism of those earthquakes and its source spectrum. When using a source with merely low-frequency content up to 10 Hz (Neuberg 2000), the resulting waveforms look similar to observed signals and the spectra match with the observed ones; however, when using a source with a broad-band spectrum, which includes frequencies up to 20 Hz, the frequency spectrum reveals a broader content than the observed spectrum of low-frequency earthquakes at Montserrat. We wonder whether high frequencies are produced at the source and damped, or whether they are not produced at the source at all. This question is important as far as the source process is concerned, however this study does not fully address the source mechanism of low-frequency earthquakes.

In summary, this study has four main objectives:

(i) to investigate the effect of anelasticity on characteristics of the frequency content and dispersion of low-frequency earthquakes;

(ii) to study the impact of topography on waveform and amplitude of low-frequency earthquakes;

(iii) to suggest a strategy to estimate intrinsic dissipation in the volcanic fluid and anelastic attenuation in the surrounding solid using low-frequency earthquakes;

(iv) to provide constraints on the rheology of volcanic media on the basis of viscoelastic wave propagation.

First, we discuss a rheological model for volcanic media, then we describe the viscoelastic formulation of the seismic wave propagation. Next, we apply this technique to the modelling of the wave field generated by the resonance in a closed system in a medium limited by a free-surface topography.

2 ATTENUATION AND DISPERSION OF SEISMIC WAVES IN VOLCANIC MEDIA

As seismic waves propagate in Earth materials, their amplitudes attenuate and their phase spectra change (Liu *et al.* 1976; Carcione *et al.* 1988), as a result of various processes, summarized as internal friction (Aki & Richards 2002). The waves within volcanic media are affected both in terms of amplitude attenuation and frequency dispersion. The glass transition is a major rheological change in the behaviour of silicate melts: change of viscosity, wave velocities, density, etc... (Dingwell 1995). Which rheological model should we choose for the range of seismic frequencies in volcanic media? Are there any *S* waves in the magma as a partially crystallized body, or when do they appear (Aki *et al.* 1978)? What is the effect of the anelastic rheology on the wave dispersion of low-frequency earthquakes?

The equations describing wave propagation in viscoelastic media can be derived in terms of the creep compliance or the stress relaxation function (Ben-Menahem & Singh 2000). In the following, we choose the stress relaxation function to describe completely the response of the medium (Carcione *et al.* 1988). Before we derive the velocity–stress formulation of the viscoelastic wave equation in Section 3, we have to choose a viscoelastic model for volcanic media. This choice will determine how the wave will attenuate and disperse. We justify in this section why the standard linear solid (SLS) (Zener 1948) can be applied as a viscoelastic model to volcanic media for most seismic frequencies. We first summarize basic concepts of rheology and the theory of viscoelasticity. We then recall some rheological models for various applications in the Earth and then we focus on our model for volcanic media.

2.1 Basics concepts of rheology and linear viscoelasticity

The theory of linear viscoelasticity is based on Boltzmann's superposition principle and is only valid for small changes in the stress and strain (Barnes *et al.* 1989). The general differential equation for 1-D linear viscoelasticity (Oldroyd 1964) is:

$$\left(1 + \alpha_1 \frac{\partial}{\partial t} + \alpha_2 \frac{\partial^2}{\partial t^2} + \cdots + \alpha_n \frac{\partial^n}{\partial t^n}\right)\sigma(t) = \left(\beta_0 + \beta_1 \frac{\partial}{\partial t} + \beta_2 \frac{\partial^2}{\partial t^2} + \cdots + \beta_m \frac{\partial^m}{\partial t^m}\right)\epsilon(t), \tag{1}$$

where σ and ϵ are the stress and strain, respectively, α_i and β_j are parameters describing the material, i and j ranging from 0 to n and m, respectively, with $n = m$ or $n = m - 1$, and $\frac{\partial^n}{\partial t^n}$ designs the nth partial derivative with respect to time t.

The range of behaviours of materials on Earth is very wide and one defines two fundamental end-member models from this equation (Barnes *et al.* 1989). If β_0 is the only non-zero parameter, we have Hooke's law. The mechanical representation of this model is a spring of rigidity $\beta_0 = \mu$. If β_1 is the only non-zero parameter, we have Newton's viscous law. The mechanical representation of this model is a dashpot of viscosity $\beta_1 = \eta$. A viscoelastic body is defined by a superposition of the above, i.e., the stress depends on the strain (elastic behaviour) as well as the rate of strain (viscous behaviour). By employing more parameters α_i and/or β_i, there is a wide range of so-called viscoelastic models. Which property dominates and the values of the parameters depend on the duration of application of the stress. Consequently, a given material can behave like a solid or like a viscous liquid, depending on the timescale of the deformation process. This is usually quantified using the dimensionless Deborah number (Reiner 1945) $D_e = \tau/T$, where T is the characteristic time of the deformation process being observed and τ is the characteristic time of the material. τ is infinite for the Hookean elastic solid and is zero for a Newtonian viscous liquid. High Deborah numbers correspond to solid-like behaviour and low Deborah numbers to liquid-like behaviour.

Two important viscoelastic bodies are the Kelvin–Voigt model (a spring and a dashpot in parallel) and the Maxwell model (a spring and a dashpot in series) (Barnes *et al.* 1989). The differential equation of the Maxwell model is obtained by choosing α_1 and β_1 as the only non-zero material parameters in eq. (1), so that

$$\sigma + \tau_M \frac{\partial \sigma}{\partial t} = \eta \frac{\partial \epsilon}{\partial t}, \tag{2}$$

where $\tau_M = \eta/\mu$ is called the relaxation time, η is the viscosity and μ is the rigidity. More complex models have been defined, which have mechanical equivalents using springs and dashpots in series and/or in parallel. Roscoe (1950) showed that all models, however complex they are, can be reduced to two fundamental forms. These are the generalized Kelvin model and the generalized Maxwell model (Barnes *et al.* 1989). As an example, the generalized Maxwell model may have a finite number of Maxwell elements in parallel, each with a different relaxation time.

2.2 The quality factor Q and lag between stress and strain

Attenuation of seismic waves is often quantified in seismology by the quality factor Q, or equivalently by the internal friction Q^{-1}, which estimates quantitatively the transformation of mechanical energy into heat, as waves propagate in the anelastic medium. The Fourier transform of the linear viscoelastic differential equation allows us to obtain a definition of the attenuation (O'Connell & Budiansky 1978) and to link Q with the lag between stress and strain and with physical properties of the material, through the relaxation functions. The Fourier transform of eq. (1) yields (Ben-Menahem & Singh 2000)

$$\tilde{\sigma}(\omega) = Y^*(i\omega)\tilde{\epsilon}(\omega) = \frac{\beta_0 + \beta_1(i\omega) + \beta_2(i\omega)^2 + \cdots + \beta_m(i\omega)^m}{1 + \alpha_1(i\omega) + \alpha_2(i\omega)^2 + \cdots + \alpha_n(i\omega)^n}\tilde{\epsilon}(\omega), \tag{3}$$

where $Y^*(i\omega)$ is the complex relaxation modulus, $\tilde{\sigma}(\omega) = \int_{-\infty}^{+\infty}\sigma(t)e^{-i\omega t}dt$, $\tilde{\epsilon}(\omega) = \int_{-\infty}^{+\infty}\epsilon(t)e^{-i\omega t}dt$, $\omega = 2\pi f$, f is the frequency, t is the time and $i^2 = -1$. Let the input strain ϵ be harmonic, i.e. $\epsilon = \epsilon_0 e^{i\omega t}$, and let the stress response be $\sigma = \sigma_0 e^{i(\omega t + \delta)}$, where δ is the phase lag between stress and strain. Inserting the Fourier transform of these expressions in eq. (3), we obtain

$$\frac{\sigma^*}{\epsilon_0} = Y^*(i\omega) = \tilde{Y}_1(\omega) + i\tilde{Y}_2(\omega), \tag{4}$$

where $\sigma^* = \sigma_0 e^{i\delta}$, $\tilde{Y}_1(\omega) = \text{Re}[Y^*(i\omega)]$, $\tilde{Y}_2(\omega) = \text{Im}[Y^*(i\omega)]$, with $\text{Re}(Z)$ and $\text{Im}(Z)$ the real and imaginary part of the complex number Z, respectively. We have

$$\frac{\sigma_0}{\epsilon_0} = |Y^*(i\omega)|, \quad \tan\delta = \frac{\tilde{Y}_2(\omega)}{\tilde{Y}_1(\omega)}. \tag{5}$$

As δ represents the lag of the stress behind the strain, a measure of the attenuation is given by the quality factor Q defined as a function of frequency by O'Connell & Budiansky (1978),

$$Q(\omega) = \frac{1}{\tan\delta} = \frac{\tilde{Y}_1(\omega)}{\tilde{Y}_2(\omega)}. \tag{6}$$

Eq. (6) defines Q as the number of wavelengths a pulse may propagate before its amplitude drops by a factor of $e^{-\pi}$ (White 1992) and defines it as a property of the material only (Madja *et al.* 1985), because the real and imaginary parts of the complex relaxation modulus are depending

on the material properties only. For a phase lag $\delta = 0$, the medium behaves elastically; for $\delta = \pi/2$, it is critically damped. Because attenuation and dispersion are related through the Kramers–Krönig relation (Futterman 1962), the choice of a physically realistic relation of Q versus frequency yields an equally physical dispersion relation (Robertsson *et al.* 1994; Blanch *et al.* 1995).

2.3 Viscoelastic models of volcanic media

Volcanic media comprise solidified material of the volcanic edifice as well as a viscous magma mixture of crystals, melt and gas in the plumbing system.

Besides theoretical studies (Caputo 1967; Madja *et al.* 1985; Caputo 1986; Dingwell 1995), there are two groups of approaches to obtain the rheology of materials.

(i) Methods using the seismic wave attenuation and dispersion in the Earth (Tonn 1989), like controlled seismic experiments (Ricker 1952; McDonal *et al.* 1958), analysis of seismic waves generated by earthquakes, i.e. body waves (Burdick 1985), surface waves (Chan & Mitchell 1985; Carcione 1992), or free modes of the Earth (Dahlen & Tromp 1998). In volcanic areas, tomography studies aim at the internal structure of the volcanoes (Wittlinger *et al.* 1983; Scherbaum 1995; Zollo *et al.* 2002), but surprisingly, little attempt has been made to obtain rheological properties of magmas. In recent studies, Kumagai & Chouet (1999, 2000a,b); Kumagai *et al.* (2002a) link the analysis of volcanic earthquakes to magma composition; Taylor & Singh (2002) assess theoretically the effect of microstructure, geometry and orientation of melt and crystals on the seismic velocities and anisotropy; Almendros *et al.* (2002) identify elements of the plumbing system beneath Kilauea volcano from the source locations of very long period signals.

(ii) Laboratory experimental studies like ultrasonic pulse propagation in samples (Wuenschel 1965; Strick 1967; Sato & Maghnani 1985; Sato *et al.* 1989; Chen 1996), or observation of forced torsional oscillations of rock samples (Kampfmann & Berckhemer 1985; Jackson & Paterson 1987; Jackson *et al.* 1992). The latter technique gives values of the shear viscosity and the shear modulus and the internal friction. The change in strain rate, confining pressure and temperature, allows us to get viscoelastic parameters as a function of frequency, pressure and temperature. Extensive measurements have been made on rock or melt samples, using both ultrasonic measurements (Vanorio *et al.* 2002) and forced torsional oscillations with or without bubbles and crystals (Bagdassarov & Dingwell 1992, 1993b; Bagdassarov *et al.* 1994; Bagdassarov & Dorfman 1998). A bubble- and crystal-free melt behaves like a Maxwell body (Dingwell 1995). The most dramatic change in rheology happens at the glass transition, where the non-Newtonian part of the rheology is the critical one. In bubbly liquids, the internal friction in the high-frequency/high-temperature range is unaffected by the presence of bubbles and depends on the bubble content in the high-temperature range (Bagdassarov & Dingwell 1992, 1993b). The viscoelastic model that describes foamed magma best is the Burgers body, the analogous mechanical model of which is shown in Fig. 2. In three-phase magmas (crystals, melt and gas), two viscoelastic behaviours can be distinguished (Bagdassarov *et al.* 1994), depending on a critical crystal concentration. In crystallizing melts without vesicles, the melt rheology is dominant below a critical crystal concentration of 45 per cent. In the presence of vesicles, this critical concentration can be higher, because bubbles can significantly decrease viscosity in the material. The mechanical interaction between crystals above this critical concentration of crystals causes a weak elastic behaviour of the magma. The experimental viscoelastic behaviour of materials is often expressed using the internal friction or the inverse of the mechanical quality factor as a function of $\omega\tau$, where $\omega = 2\pi f$ angular frequency in (rad s^{-1}) and τ is the relaxation time. Bagdassarov *et al.* (1994) showed that the behaviour of volcanic products is different when $\omega\tau < 1$ or when $\omega\tau > 1$.

Now, the main question is how these viscoelastic models are used to describe the behaviour of volcanic media at seismic frequencies. At Montserrat, installed seismometers are able to record seismic waves within a frequency range 0.02 to 25 Hz, corresponding to relaxation times $\tau = 1/(2\pi f)$ ranging 0.0064 s to approximately 8 s. *S* waves start to appear in the crystallizing magma from 45 per cent of crystals, because the shear modulus becomes non-zero (Bagdassarov *et al.* 1994). Accordingly, those models where crystals are present behave more elastically than viscously. Bagdassarov *et al.* (1994) showed that when $\omega\tau > 1$, the melt itself possesses more elasticity than the ideal viscoelastic Maxwell
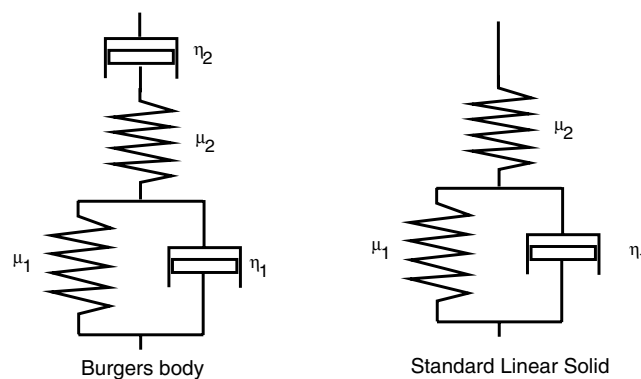
Figure 2. Mechanical models for (a) a Burgers body and (b) a standard linear solid (SLS). At seismic frequencies, the viscosity controlling the long timescale vanishes and the two models are equivalent.

liquid. A foamed rhyolitic melt behaves like a Burgers body (Bagdassarov & Dingwell 1993a), which is characterized by two viscosities (Fig. 2), one controlling short-timescale processes and the other controlling the long-timescale behaviour (Ranalli 1995). For seismic waves (short-timescale processes), the viscosity controlling the long-timescale process becomes infinite, because there is no time to reach a strain regime, where the melt starts to relax (Dingwell 1995). This is equivalent to a frozen dashpot. Consequently, the viscoelastic behaviour of a foamed rhyolite has the characteristics of an SLS provided the frequency considered is larger than 2 Hz. We assume that both magma and surrounding rocks behave like it (Fig. 2).

2.4 The standard linear solid

The mechanical analogue of the SLS (Zener 1948) consists of spring of rigidity μ_1 and a dashpot of viscosity η_1 in parallel, in series with a spring of rigidity μ_2 (Fig. 2). In 1-D, it is governed by

$$\sigma + \tau_\sigma \frac{\partial \sigma}{\partial t} = M_R \left(\epsilon + \tau_\epsilon \frac{\partial \epsilon}{\partial t} \right), \tag{7}$$

where the relaxation modulus of the medium is $M_R = \mu_1 \mu_2 / (\mu_1 + \mu_2)$, the stress relaxation time under constant strain is $\tau_\sigma = \eta_1 / (\mu_1 + \mu_2)$ and the strain relaxation time under constant stress is $\tau_\epsilon = \eta_1 / \mu_1 > \tau_\sigma$. The solution of eq. (7) for $\epsilon = \epsilon_0 H(t)$ is given by $\sigma(0) = \mu_2 \epsilon_0$, $\sigma(\infty) = M_R \epsilon_0$ and $\sigma(t) = \epsilon_0 G_1(t)$, where the stress relaxation function $G_1(t)$ is given (Liu *et al.* 1976; Blanch *et al.* 1995) by

$$G_1(t) = M_R \left[1 - \left(1 - \frac{\tau_\epsilon}{\tau_\sigma} \right) e^{-t/\tau_\sigma} \right] H(t), \tag{8}$$

where $H(t)$ is the Heavyside step function. The response to a harmonic stress cycle is obtained by setting $\sigma = S e^{i\omega t}$ and $\epsilon = E e^{i\omega t}$ in eq. (7) to obtain

$$\frac{S}{E} = M_R \frac{1 + i\omega \tau_\epsilon}{1 + i\omega \tau_\sigma} = \mu_2 \frac{\mu_1 + i\omega \eta_1}{(\mu_1 + \mu_2) + i\omega \eta_1} = K e^{i\delta}, \tag{9}$$

where E, S and K are constants, and

$$Q(\omega) = \frac{1}{\tan \delta} = \frac{1 + \omega^2 \tau_\epsilon \tau_\sigma}{\omega(\tau_\epsilon - \tau_\sigma)}. \tag{10}$$

The phase velocity (for an SLS with one relaxation mechanism) is given by (Ben-Menahem & Singh 2000)

$$\frac{c(\omega)}{c(0)} = \sqrt{\frac{2[1 + \omega^2 \tau_0^2 (\tau_\epsilon / \tau_\sigma)]}{\sqrt{[(1 + \omega^2 \tau_0^2)^2 + 4\omega^2 \tau_0^2 Q_0^{-2}]} + 1 + \omega^2 \tau_0^2}}, \tag{11}$$

in which $c(0) = \sqrt{M_R / \rho}$ is the elastic velocity (ρ being the density) and where $Q_0^{-1} = (\tau_\epsilon - \tau_\sigma)/(2\tau_0)$, $\tau_0 = \sqrt{\tau_\epsilon \tau_\sigma}$..

   One relaxation mechanism is usually not sufficient to reproduce the rheological behaviour of materials and consequently the introduction of several mechanisms in series or in parallel has been proposed (Barnes *et al.* 1989). For an array of L SLS, the stress relaxation function

$$G_L(t) = M_R \left[1 - \sum_{l=1}^{L} \left(1 - \frac{\tau_{\epsilon l}}{\tau_{\sigma l}} \right) e^{-t/\tau_{\sigma l}} \right] H(t) \tag{12}$$

makes it possible to get a macroscopic model of anelasticity (Ben-Menahem & Singh 2000). For example, a way to model a frequency-independent attenuation is to associate several SLS in parallel (Blanch *et al.* 1995). For an array of SLS with L relaxation mechanisms, eqs (12) and (6) yield (Blanch *et al.* 1995),

$$Q(\omega) = \frac{1 - L + \sum_{l=1}^{L} \frac{1 + \omega^2 \tau_{\epsilon l} \tau_{\sigma l}}{1 + \omega^2 \tau_{\sigma l}^2}}{\sum_{l=1}^{L} \frac{\omega(\tau_{\epsilon l} - \tau_{\sigma l})}{1 + \omega^2 \tau_{\sigma l}^2}}. \tag{13}$$

   From here, it is possible to get any Q dependence with frequency, by adjusting the stress relaxation times distribution of the L relaxation mechanisms, as needed. Attenuation is generally frequency-dependent (Aki 1980; Bourbie *et al.* 1987; Patane *et al.* 1994) and varies with depth. McDonal *et al.* (1958) argue that attenuation is constant within the seismic frequency range (1–200 Hz) and many studies use the constant Q approximation, e.g. in tomography (Wittlinger *et al.* 1983; Scherbaum 1995) and in exploration seismology (Robertsson *et al.* 1994; Blanch *et al.* 1995). For a sufficiently well chosen repartition of stress relaxation times and a desired frequency band, eq. (13) gives a constant Q (Blanch *et al.* 1995). We use this approach in our modelling. Note that, in the case of a homogeneous and isotropic medium, we can define two independent quality factors Q_P and Q_S from eq. (13), using two series of SLS, associated with the attenuation of P waves and S waves, respectively. Assuming a constant Q between two frequencies $f_1 = \omega_1 / 2\pi$ and $f_2 = \omega_2 / 2\pi$ and defining $s_1 = 1/\omega_1$ and $s_2 = 1/\omega_2$, the phase velocity $c(\omega)$ is given by (Ben-Menahem & Singh 2000)

$$\frac{c(\infty)}{c(\omega)} = 1 + \frac{1}{2\pi Q} \ln \frac{\omega^2 + s_2^2}{\omega^2 + s_1^2}, \tag{14}$$

where

$$c(\infty) = c(0) \left(1 + \frac{1}{\pi Q} \ln \frac{s_2}{s_1} \right), \tag{15}$$

where $c(0)$ is again the elastic velocity.

Finally, we give the order of magnitude of the quality factor given by SLS models for properties corresponding to various magmas. Values of Q in volcanic areas are lower than elsewhere on Earth, with values ranging from 20 to 200 (Zucca & Evans 1992). Experimental studies on pyroclastic and lava samples (Vanorio *et al.* 2002) give values of Q_P ranging from 5 to 80 and 10 to 115, respectively. In basaltic melt samples, $Q_P = 2$–15 (Sato & Maghnani 1985). For one SLS mechanism (Fig. 2) and using the dtions of the stress relaxation time under constant strain $\tau_\sigma = \eta_1/(\mu_1 + \mu_2)$ and the strain relaxation time under constant stress $\tau_\epsilon = \eta_1/\mu_1 > \tau_\sigma$, Q is related to viscosity η_1 and rigidities μ_1 and μ_2 of the media via the relaxation times (eq. 10),

$$Q(\omega) = \frac{\mu_1}{\mu_2}(\mu_1 + \mu_2)\frac{1}{\eta_1\omega} + \frac{\eta_1\omega}{\mu_1}. \tag{16}$$

Depending on the frequency and the rigidity values, the quality factor can have any value ($Q < 5$ to $Q \gg 10\,000$), for viscosity values of rhyolitic crystallizing magmas ranging from 6.4×10^4 to 1.7×10^7 Pa s, respectively (Barmin *et al.* 2002), and also for higher viscosities like those measured at Montserrat, which range between 10^9 and 10^{14} Pa s (Sparks *et al.* 2000). This shows that the SLS is able to quantify intrinsic attenuation of seismic waves for volcanic media via the quality factor Q.

3 VISCOELASTIC FINITE-DIFFERENCE WAVE PROPAGATION FORMULATION WITH TOPOGRAPHY

Several modelling methods for wave propagation, which take attenuating and dispersion effects into account, have been proposed (Carcione 1993; Carcione *et al.* 2002). We use a 2-D finite-difference velocity–stress time domain formulation (Virieux 1986; Levander 1988) of the viscoelastic wave equations (Robertsson *et al.* 1994), in a heterogeneous medium with a non-flat free-surface topography (Hestholm & Ruud 2000). This formulation comprises (i) the *P-SV* equation of motion; (ii) constitutive laws; (iii) equations for memory functions. We describe first how topography is modelled, then we derive the velocity–stress formulation of the wave equations for an isotropic homogeneous viscoelastic medium, modelled by a series of SLS, and the formulation of the specific boundary condition for the free-surface. Finally, we detail the discretization and implementation of this series of equations.

3.1 Topography

The incorporation of surface topography is achieved by using a linear mapping transformation (Fig. 3) of the rectangular computational grid onto a curved grid (Tessmer *et al.* 1992). The 2-D mapping function can be written as

$$x(\zeta, \eta) = \zeta,$$
$$z(\zeta, \eta) = \frac{\eta}{\eta_{max}}z_0(\zeta), \tag{17}$$

where $z_0(\zeta)$ is the topography function, and the rectangular (ζ, η)-system is bounded by $\zeta = 0$, $\zeta = \zeta_{max}$, $\eta = 0$ and $\eta = \eta_{max}$. For a curved profile in the (x, z) system, the extent of stretching is proportional to the distance from the bottom edge of the grid. For any $F(x, z)$ function representing the distribution of any physical property or field in the medium, the equations for the linear mapping transformation are

$$\frac{\partial F}{\partial x} = \frac{\partial F}{\partial \zeta} + A(\zeta, \eta)\frac{\partial F}{\partial \eta},$$
$$\frac{\partial F}{\partial z} = B(\zeta)\frac{\partial F}{\partial \eta},$$

with

$$A(\zeta, \eta) = -\frac{\eta}{z_0(\zeta)}\frac{\partial z_0(\zeta)}{\partial \zeta}, \tag{18}$$
$$B(\zeta) = \frac{\eta_{max}}{z_0(\zeta)},$$

where ζ, η are the coordinates in the computational grid (Hestholm & Ruud 2000; Ruud & Hestholm 2001).

3.2 *P-SV* wave equation of motion

The equations of motion for the *P-SV* wave equation are

$$\rho\frac{\partial v_x}{\partial t} = \frac{\partial \sigma_{xx}}{\partial x} + \frac{\partial \sigma_{xz}}{\partial z},$$
$$\rho\frac{\partial v_z}{\partial t} = \frac{\partial \sigma_{xz}}{\partial x} + \frac{\partial \sigma_{zz}}{\partial z}, \tag{19}$$

where ρ is the density, v_x and v_z are the horizontal and vertical components of the velocity, respectively, and σ_{xx}, σ_{zz} and σ_{xz} are the two normal and one tangential components of the stress field, respectively. Replacing the linear mapping eq. (18) into the equations of motions
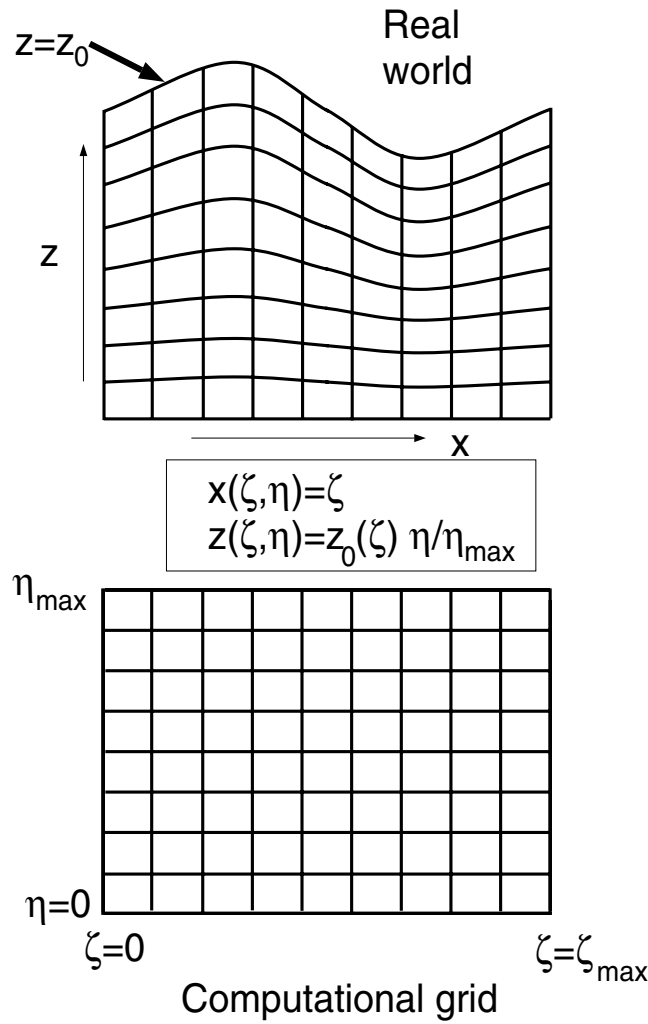
Figure 3. Curved grid in the (x, z) system and rectangular grid in the (ζ, η) system.

(19) yields

$$\rho \frac{\partial v_x}{\partial t} = \frac{\partial \sigma_{xx}}{\partial \zeta} + A(\zeta, \eta) \frac{\partial \sigma_{xx}}{\partial \eta} + B(\zeta) \frac{\partial \sigma_{xz}}{\partial \eta},$$

$$\rho \frac{\partial v_z}{\partial t} = \frac{\partial \sigma_{xz}}{\partial \zeta} + A(\zeta, \eta) \frac{\partial \sigma_{xz}}{\partial \eta} + B(\zeta) \frac{\partial \sigma_{zz}}{\partial \eta}. \tag{20}$$

3.3 Tensor formulation of the linear viscoelastic constitutive relationship

We proceed now to the derivation of the constitutive relationship, using the SLS as a rheological model. The tensor formulation of linear viscoelasticity (eq. 1) is embodied in Boltzmann's superposition principle where the stress tensor (noted by its component σ_{ij}) depends on the history of the strain tensor (noted by its component ϵ_{kl}) and can be described as (Christensen 2004)

$$\sigma_{ij} = G_{ijkl} * \frac{\partial \epsilon_{kl}}{\partial t} = \frac{\partial G_{ijkl}}{\partial t} * \epsilon_{kl}, \tag{21}$$

where * denotes time convolution. Each strain history $\partial \epsilon_{kl}/\partial t$ is transformed into the current stress value, $\sigma_{ij}(t)$. G_{ijkl} denotes the component of a fourth-order tensor **G** of stress relaxation functions, which is analogous to the elasticity tensor.

For an isotropic and homogeneous material, **G** collapses into two independent functions Λ and $2M$. The constitutive relationship simplifies to (Christensen 2004)

$$\sigma_{ij} = \frac{\partial \Lambda}{\partial t} * \delta_{ij} \epsilon_{kk} + 2 \frac{\partial M}{\partial t} * \epsilon_{ij}, \tag{22}$$

where δ_{ij} is the Kronecker delta and Einstein's summation convention is used. Λ is called the longitudinal relaxation function and M is called the shear relaxation function (Madja *et al.* 1985). Using the time derivative of the strain tensor,

$$\frac{\partial \epsilon_{ij}}{\partial t} = \frac{1}{2}\left(\frac{\partial v_i}{\partial x_j} + \frac{\partial v_j}{\partial x_i}\right), \tag{23}$$

where v_i and v_j are the velocity components in the x_i and x_j directions respectively and, using $\Gamma = \Lambda + 2M$, Robertsson *et al.* (1994) and Hestholm (1999) obtained from the constitutive relationship (eq. 22)

$$\frac{\partial \sigma_{ii}}{\partial t} = \left(\frac{\partial \Gamma}{\partial t} - 2\frac{\partial M}{\partial t}\right) * \frac{\partial v_k}{\partial x_k} + 2\frac{\partial M}{\partial t} * \frac{\partial v_i}{\partial x_i},$$

$$\frac{\partial \sigma_{ij}}{\partial t} = \frac{\partial M}{\partial t} * \left(\frac{\partial v_i}{\partial x_j} + \frac{\partial v_j}{\partial x_i}\right), i \neq j, \tag{24}$$

in which we used the property that the time derivative of the convolution between two functions g and f is $\partial(f * g)/\partial t = (\partial f/\partial t) * g = f * (\partial g/\partial t)$. In the case of a series of L SLS as a rheological model (eq. 12), Γ and M are given by

$$\Gamma = \gamma\left[1 - \sum_{l=1}^{L}\left(1 - \frac{\tau_{\epsilon l}^P}{\tau_{\sigma l}}\right)e^{-t/\tau_{\sigma l}}\right]H(t),$$

$$M = \mu\left[1 - \sum_{l=1}^{L}\left(1 - \frac{\tau_{\epsilon l}^S}{\tau_{\sigma l}}\right)e^{-t/\tau_{\sigma l}}\right]H(t), \tag{25}$$

where $\gamma = \lambda + 2\mu$, λ and μ are the elastic Lamé parameters and L is the number of SLS connected in parallel. $\tau_{\sigma l}$ and $\tau_{\epsilon l}$ are the stress and strain relaxation times for the lth mechanism (Pipkin 1986). The two relaxation functions Γ and M depend on the strain relaxation time $\tau_{\epsilon l}^P$ for P waves and on the strain relaxation time $\tau_{\epsilon l}^S$ for S waves, respectively.

We perform the time differentiation of Γ and M (eq. 25) and introduce them in the constitutive relationships (eq. 24) to obtain

$$\frac{\partial \sigma_{xx}}{\partial t} = \gamma S_L^P\left(\frac{\partial v_x}{\partial x} + \frac{\partial v_z}{\partial z}\right) - 2\mu S_L^S\frac{\partial v_z}{\partial z} + S_{Lxx},$$

$$\frac{\partial \sigma_{zz}}{\partial t} = \gamma S_L^P\left(\frac{\partial v_x}{\partial x} + \frac{\partial v_z}{\partial z}\right) - 2\mu S_L^S\frac{\partial v_x}{\partial x} + S_{Lzz}, \tag{26}$$

$$\frac{\partial \sigma_{xz}}{\partial t} = \mu S_L^S\left(\frac{\partial v_x}{\partial z} + \frac{\partial v_z}{\partial x}\right) + S_{Lxz},$$

where

$$S_L^P = \left(1 - \sum_{l=1}^{L}\left(1 - \frac{\tau_{\epsilon l}^P}{\tau_{\sigma l}}\right)\right),$$

$$S_L^S = \left(1 - \sum_{l=1}^{L}\left(1 - \frac{\tau_{\epsilon l}^S}{\tau_{\sigma l}}\right)\right), \tag{27}$$

$$S_{Lij} = \sum_{l=1}^{L} r_{ijl}, \text{ with } i, j \iff x, z,$$

and where r_{xxl}, r_{zzl} and r_{xzl} are the memory variables that are defined in Section 3.4. We introduce now the linear mapping eqs (18) of the topography, yielding

$$\frac{\partial \sigma_{xx}}{\partial t} = \gamma S_L^P\left[\frac{\partial v_x}{\partial \zeta} + A(\zeta, \eta)\frac{\partial v_x}{\partial \eta} + B(\zeta)\frac{\partial v_z}{\partial \eta}\right] - 2\mu S_L^S B(\zeta)\frac{\partial v_z}{\partial \eta} + S_{Lxx},$$

$$\frac{\partial \sigma_{zz}}{\partial t} = \gamma S_L^P\left[\frac{\partial v_x}{\partial \zeta} + A(\zeta, \eta)\frac{\partial v_x}{\partial \eta} + B(\zeta)\frac{\partial v_z}{\partial \eta}\right] - 2\mu S_L^S\left[\frac{\partial v_x}{\partial \zeta} + A(\zeta, \eta)\frac{\partial v_x}{\partial \eta}\right] + S_{Lzz}, \tag{28}$$

$$\frac{\partial \sigma_{xz}}{\partial t} = \mu S_L^S\left[B(\zeta)\frac{\partial v_x}{\partial \eta} + \frac{\partial v_z}{\partial \zeta} + A(\zeta, \eta)\frac{\partial v_z}{\partial \eta}\right] + S_{Lxz}.$$

3.4 Relaxation equations

In eq. (26), we introduced the memory variables, in which we perform now a new time derivative (Robertsson *et al.* 1994; Hestholm & Ruud 2000) to obtain

$$\frac{\partial r_{xx,l}}{\partial t} = -\frac{1}{\tau_{\sigma l}} \left\{ r_{xx,l} + \left[\gamma \left(\frac{\tau_{\epsilon l}^P}{\tau_{\sigma l}} - 1 \right) - 2\mu \left(\frac{\tau_{\epsilon l}^S}{\tau_{\sigma l}} - 1 \right) \right] \left(\frac{\partial v_x}{\partial x} + \frac{\partial v_z}{\partial z} \right) + 2\mu \left(\frac{\tau_{\epsilon l}^S}{\tau_{\sigma l}} - 1 \right) \frac{\partial v_x}{\partial x} \right\},$$

$$\frac{\partial r_{zz,l}}{\partial t} = -\frac{1}{\tau_{\sigma l}} \left\{ r_{zz,l} + \left[\gamma \left(\frac{\tau_{\epsilon l}^P}{\tau_{\sigma l}} - 1 \right) - 2\mu \left(\frac{\tau_{\epsilon l}^S}{\tau_{\sigma l}} - 1 \right) \right] \left(\frac{\partial v_x}{\partial x} + \frac{\partial v_z}{\partial z} \right) + 2\mu \left(\frac{\tau_{\epsilon l}^S}{\tau_{\sigma l}} - 1 \right) \frac{\partial v_z}{\partial z} \right\}, \qquad (29)$$

$$\frac{\partial r_{xz,l}}{\partial t} = -\frac{1}{\tau_{\sigma l}} \left[r_{xz,l} + \mu \left(\frac{\tau_{\epsilon l}^S}{\tau_{\sigma l}} - 1 \right) \left(\frac{\partial v_x}{\partial z} + \frac{\partial v_z}{\partial x} \right) \right].$$

Defining

$$\tau_l^P = -\frac{1}{\tau_{\sigma l}} \left(\frac{\tau_{\epsilon l}^P}{\tau_{\sigma l}} - 1 \right),$$

$$\tau_l^S = -\frac{1}{\tau_{\sigma l}} \left(\frac{\tau_{\epsilon l}^S}{\tau_{\sigma l}} - 1 \right), \qquad (30)$$

the relaxation eq. (29) can then be written as

$$\frac{\partial r_{xx,l}}{\partial t} = -\frac{r_{xx,l}}{\tau_{\sigma l}} + \gamma \tau_l^P \left(\frac{\partial v_x}{\partial x} + \frac{\partial v_z}{\partial z} \right) - 2\mu \tau_l^S \frac{\partial v_z}{\partial z},$$

$$\frac{\partial r_{zz,l}}{\partial t} = -\frac{r_{zz,l}}{\tau_{\sigma l}} + \gamma \tau_l^P \left(\frac{\partial v_x}{\partial x} + \frac{\partial v_z}{\partial z} \right) - 2\mu \tau_l^S \frac{\partial v_x}{\partial x}, \qquad (31)$$

$$\frac{\partial r_{xz,l}}{\partial t} = -\frac{r_{xz,l}}{\tau_{\sigma l}} + \mu \tau_l^S \left(\frac{\partial v_x}{\partial z} + \frac{\partial v_z}{\partial x} \right).$$

We introduce now the linear mapping eq. (18) of the topography. This leads us to the following equations:

$$\frac{\partial r_{xx,l}}{\partial t} = -\frac{r_{xx,l}}{\tau_{\sigma l}} + \gamma \tau_l^P \left[\frac{\partial v_x}{\partial \zeta} + A(\zeta, \eta) \frac{\partial v_x}{\partial \eta} + B(\zeta) \frac{\partial v_z}{\partial \eta} \right] - 2\mu \tau_l^S \left(B(\zeta) \frac{\partial v_z}{\partial \eta} \right),$$

$$\frac{\partial r_{zz,l}}{\partial t} = -\frac{r_{zz,l}}{\tau_{\sigma l}} + \gamma \tau_l^P \left[\frac{\partial v_x}{\partial \zeta} + A(\zeta, \eta) \frac{\partial v_x}{\partial \eta} + B(\zeta) \frac{\partial v_z}{\partial \eta} \right] - 2\mu \tau_l^S \left[\frac{\partial v_x}{\partial \zeta} + A(\zeta, \eta) \frac{\partial v_x}{\partial \eta} \right], \qquad (32)$$

$$\frac{\partial r_{xz,l}}{\partial t} = -\frac{r_{xz,l}}{\tau_{\sigma l}} + \mu \tau_l^S \left[B(\zeta) \frac{\partial v_x}{\partial \eta} + \frac{\partial v_z}{\partial \zeta} + A(\zeta, \eta) \frac{\partial v_z}{\partial \eta} \right].$$

The system of eqs (20), (28) and (32) consists of the system to be solved to model the 2-D wave propagation in an isotropic and homogeneous viscoelastic medium, in which the attenuation is modelled by a number *L* of SLSs in parallel and bounded by a free-surface topography.

3.5 Specific free-surface boundary conditions

At the free surface, the traction vector **T** vanishes, i.e.

$$\mathbf{T} = \Sigma \cdot \mathbf{n} = \mathbf{0}, \qquad (33)$$

i.e. in components,

$$\sigma_{ij} n_j = 0, \qquad (34)$$

where Σ is the stress tensor with components σ_{ij} and **n** is a normal vector to the local surface point with components n_j; $i, j = 1, 2$. Any normal vector may be used, even though **T** is defined by the unit normal vector. In 2-D, we can choose

$$\mathbf{n} = \left(-\frac{\partial z_0(\zeta)}{\partial \zeta}, 1\right)^{\mathrm{T}} = (-\tan\phi, 1)^{\mathrm{T}}, \tag{35}$$

where ϕ denotes the local topography slope angle and the superscript indicates the transpose. Using components, the condition (34) becomes

$$-\sigma_{xx}\tan\phi + \sigma_{xz} = 0,$$
$$-\sigma_{xz}\tan\phi + \sigma_{zz} = 0, \tag{36}$$

with σ_{xx}, σ_{xz} and σ_{zz} denoting the stress components. Differentiating with respect to time yields

$$-\frac{\partial \sigma_{xx}}{\partial t}\tan\phi + \frac{\partial \sigma_{xz}}{\partial t} = 0,$$
$$-\frac{\partial \sigma_{xz}}{\partial t}\tan\phi + \frac{\partial \sigma_{zz}}{\partial t} = 0. \tag{37}$$

The substitution for $\partial \sigma_{xx}/\partial t$, $\partial \sigma_{xz}/\partial t$ and $\partial \sigma_{zz}/\partial t$ from eq. (26) is carried out in eq. (37) in three steps:

(i) the limit of an elastic medium is assumed at the surface (Robertsson 1996), i.e. $\tau_\epsilon = \tau_\sigma$ for both P and S waves and $r_{xx} = r_{zz} = r_{xz} = 0$;
(ii) we note from eq. (18) that $A(\zeta, \eta) = -B(\zeta)\tan\phi$; and
(iii) we note that $\tan\phi = \partial z_0(\zeta)/\partial\zeta$.

Performing the complete calculations, Hestholm & Ruud (2000) found the 2-D boundary condition for free-surface topography, given in the computational (ζ, η) grid by

$$B(\zeta)\left\{1 + \left[\frac{\partial z_0(\zeta)}{\partial \zeta}\right]^2\right\}\frac{\partial v_x}{\partial \eta} + B(\zeta)\frac{\partial z_0(\zeta)}{\partial \zeta}\left\{1 + \left[\frac{\partial z_0(\zeta)}{\partial \zeta}\right]^2\right\}\frac{\partial v_z}{\partial \eta} = 2\frac{\partial z_0(\zeta)}{\partial \zeta}\frac{\partial v_x}{\partial \zeta} + \left\{\left[\frac{\partial z_0(\zeta)}{\partial \zeta}\right]^2 - 1\right\}\frac{\partial v_z}{\partial \zeta},$$

$$-B(\zeta)\frac{\partial z_0(\zeta)}{\partial \zeta}\left\{1 + \left[\frac{\partial z_0(\zeta)}{\partial \zeta}\right]^2\right\}\frac{\partial v_x}{\partial \eta} + B(\zeta)\left\{1 + \left[\frac{\partial z_0(\zeta)}{\partial \zeta}\right]^2\right\}\frac{\partial v_z}{\partial \eta} = -\left\{\frac{\lambda}{\lambda + 2\mu} + \left[\frac{\partial z_0(\zeta)}{\partial \zeta}\right]^2\right\}\frac{\partial v_x}{\partial \zeta} + \frac{\partial z_0(\zeta)}{\partial \zeta}\left(1 - \frac{\lambda}{\lambda + 2\mu}\right)\frac{\partial v_z}{\partial \zeta}. \tag{38}$$

Equations of eq. (38) are exact 2-D boundary conditions for an arbitrary, smooth, free-surface topography (Hestholm & Ruud 2000). Several other formulations of the same boundary conditions can be obtained both in 2-D and 3-D and they are equivalent (Hestholm 1999; Ruud & Hestholm 2001; Hestholm 2002). In the derivation of all forms, $\mu \neq 0$ is assumed, so the conditions cannot be used for strictly acoustic cases. Note that they cannot be used for vertical subsections, because then $\tan\phi$ goes to infinity. Under these constraints, the system of equations are spacially unconditionally stable when discretized by second-order finite differences (FDs) (Ruud & Hestholm 2001).

3.6 Discretization, implementation and dispersion of the finite-difference scheme

We use a finite-difference scheme (fourth order in space and second order in time) to discretize the previous equation system, on a staggered grid both in space and time (Levander 1988; Robertsson *et al.* 1994; Carcione *et al.* 2002). At an initial time, we introduce a pressure change to the computed normal stress of the gridpoint where the source is located, according to time-dependent functions as shown in Fig. 4, and having a known amplitude. We update first the velocity fields according to the discretized versions of the wave equation of motion (eq. 20). Stress fields are updated using the discretized versions of the constitutive laws (eq. 28), is which the terms S_{Lxx}, S_{Lzz} and S_{Lxz} are approximated using a Crank–Nicholson first-order centred finite-difference scheme. The relaxation functions are updated using the discretized versions of the relaxation functions (eq. 32). We use second-order finite-difference to discretize the free-surface boundary conditions (eq. 38). Ruud & Hestholm (2001) gave a detailed description for the discretization of the free-surface topography and showed that it was unconditionally stable. Absorbing boundary conditions are defined at the three other sides of the grid using a paraxial approximation of the elastic wave equation at the boundary (Clayton & Engquist 1977) and by setting a linear decay of Q within a damping zone, from the value of Q in the solid to $Q = 2$ at the grid sides.

By computing the wave propagation numerically, we have to deal with the trade-off between accuracy and computation time. Similarly to the elastic discretization, the stability criteria for the conditional scheme we use (Robertsson *et al.* 1994) are similar to analogue elastic schemes (Levander 1988). The Courant number $c\Delta t/\Delta x$ (where c is the velocity) has to be adjusted to the highest phase velocity, which is found at infinite frequency, $c_{\max} = \sqrt{\tau_\epsilon M_R/\tau_\sigma \rho}$. For an SLS with one relaxation mechanism, this expression simplifies to $c_{\max} = \sqrt{\mu_2/\rho}$ (see Section 2.4 for notations).

Viscoelastic media are intrinsically dispersive (Aki & Richards 2002), the phase velocity increases with frequency as shown by Futterman (1962) and Wuenschel (1965). In addition, finite-difference methods for wave propagation introduce numerical dispersion because of the time and space discretization. The viscoelastic dispersion curves demonstrate the same characteristics as their elastic analogues and the damping curves are found to be very similar for different values of the Courant number and the maximum attenuation is found at 40 Hz (Levander 1988; Robertsson *et al.* 1994). Robertsson *et al.* (1994) carried out a detailed dispersion analysis and gave an empirical rule for frequencies up to 500 Hz. A minimum of eight gridpoints per wavelength is necessary to obtain less than 2 per cent of dispersion error, for a Courant
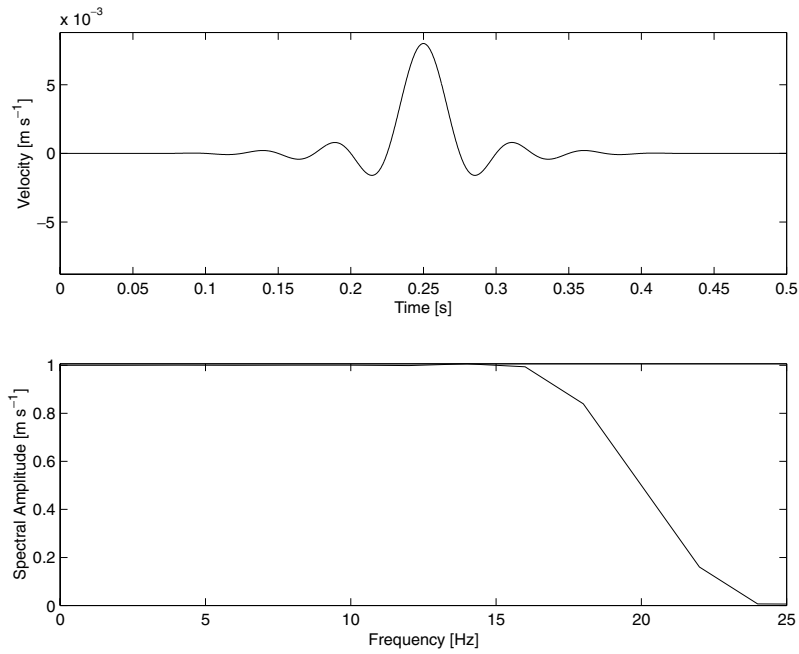
Figure 4. Source used in our modelling. (top) Time history of the source and (bottom) its corresponding amplitude spectrum.

number ranging from the stability limit to a fifth of the stability limit and for Q ranging from 10 to 10 000. The Courant number drops to 4, when a dispersion error of 5 per cent is sufficient. According to the dispersion analysis (Robertsson *et al.* 1994), the grid spacing dx must verify $dx < \frac{V}{8f}$, for a wave of frequency f that travels with a velocity V. Neuberg & O'Gorman (2002) and Sturton & Neuberg (2003) showed that the velocities in bubbly magma may be as low as 200 m s^{-1}. In order to have less than 2 per cent dispersion error in our modelling, the propagation of a wave of 25 Hz travelling in the area of the grid that has magma properties requires the grid spacing to be less than 0.5 m. This upper limit is 1 m for a 5 per cent dispersion error. All the waves we model have a frequency content lower than 25 Hz. Using a 2-m grid spacing, the maximum possible wave frequency to ensure an error on dispersion less than 2 per cent is 12.5 and 25 Hz for a wave velocity of 200 and 400 m s^{-1}, respectively. Using velocities in magma greater than 400 m s^{-1} ensures a dispersion error less than 2 per cent for a grid spacing of 2 m and using velocities in magma greater than 1000 m s^{-1} ensures a dispersion error less than 2 per cent for a grid spacing of 6 m. This analysis shows that the formulation we use is suitable to fulfill most cases with an error on dispersion between 2 and 5 per cent (depending on frequencies), using a grid spacing of 2 m and within reasonable computation time on Sun Ultra 5/10 Sparc work stations or Linux PC.

3.7 Results in homogeneous medium

When constant-Q absorption operates, the amplitude spectrum of a seismic pulse at frequency f obeys (White 1992):

$$|A_t(f)| = \frac{|A_0(f)|}{J} e^{\frac{-\pi f t}{Q}}, \tag{39}$$

where t is the traveltime of the pulse from time zero and $|A_0(f)|$ is the unattenuated amplitude spectrum of the pulse, and J^{-1} is the geometrical spreading; for body waves and in 2-D, $J = \sqrt{r}$, r being the distance from the source. Q can be estimated from the amplitude spectra $A_1(f)$ and $A_2(f)$ of the wavelet at the distances r_1 and r_2 from the source, at times t_1 and t_2, respectively, using

$$Q(f) = \frac{-\pi f(t_2 - t_1)}{\ln \frac{|A_2(f)|\sqrt{(r_2)}}{|A_1(f)|\sqrt{(r_1)}}}, \tag{40}$$

where $\ln r$ is the natural logarithm or the real positive number r.

We computed a series of seismograms in the homogeneous medium and at the free surface to evaluate the accuracy of our code in retrieving the input Q value for a P wave in a homogeneous medium. The used source has the characteristics shown in Fig. 4. We recorded synthetic P waves at one initial station R_0 and at several receivers R_i located at distances d_0 and d_i from the source, respectively. Fig. 5 shows that the quality factor can be retrieved within approximately 10–20 per cent from synthetic data recorded at the free surface, for any number of relaxation mechanisms. When the number of SLS is larger than one, the viscoelastic medium has a quality factor $Q = 50$ between 2 and 25 Hz (eq. 13), and the phase velocity is given by eq. (14). The number of relaxation mechanisms is therefore not critical for a good modelling
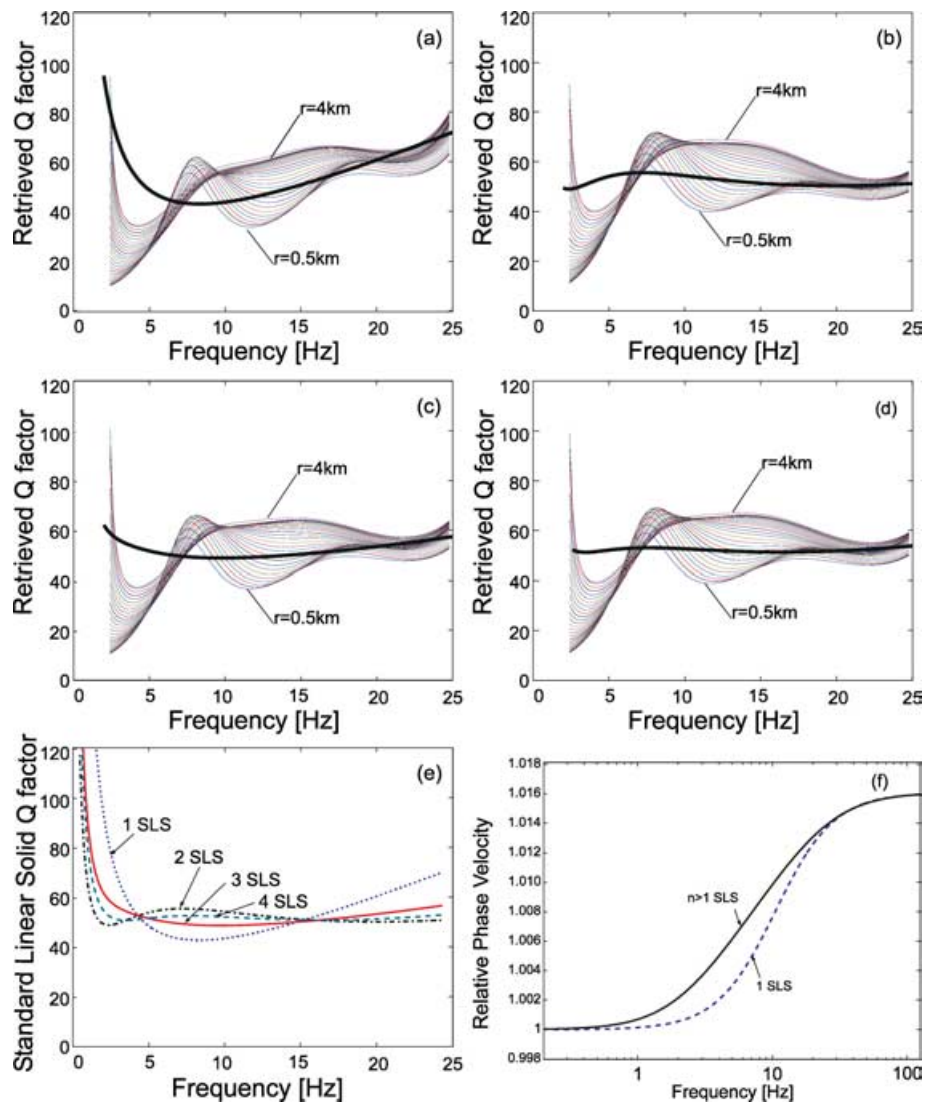
Figure 5. Quality factor retrieved from spectral amplitude ratio using seismograms recorded at various distances ($r = 0.5$ to 4 km) at the flat free surface of a homogeneous half-space with $Q = 50$ and for (a) one, (b) two, (c) three and (d) four relaxation mechanisms. Distributions of relaxation times are $\tau_\sigma(1) = [0.0187]$, $\tau_\sigma(2) = [0.0064, 0.0796]$, $\tau_\sigma(3) = [0.0064, 0.0181, 0.0796]$ and $\tau_\sigma(4) = [0.0064, 0.0074, 0.0503, 0.0796]$, respectively. (e) Quality factors represented in the same plot and (f) corresponding phase velocity for those mechanisms. Note that because the source length is 0.5 s, amplitude ratios were computed using the Fourier transform of synthetic signals having zero amplitude at frequencies below 2 Hz.

of attenuation; the synthetic seismic signals are very similar when the number of relaxation mechanisms is changed (Robertsson *et al.* 1994). In the following, unless otherwise stated, we use three relaxation mechanisms (Fig. 5), which give a good accuracy/computation time ratio.

4 2-D MODELLING OF LOW-FREQUENCY VOLCANIC EARTHQUAKES IN ANELASTIC MEDIA

4.1 Description of the models and synthetic data

In order to understand the features of low-frequency volcanic earthquakes (Fig. 1), we use simplified models of the volcanic structure. Our models consist of a rectangular conduit, filled with a viscoelastic fluid, which is embedded in a homogeneous elastic or viscoelastic solid limited by a stress-free surface with or without topography (Fig. 6). The frequency content and the dispersion of synthetic seismograms depend on the contrast between the physical properties at the conduit wall and on the geometry of the conduit (Neuberg 2000; Jousset *et al.* 2003; Sturton & Neuberg 2003). To investigate the effect of attenuation and topography, we used model parameters that produce a typical synthetic low-frequency seismogram, as observed on Montserrat. We fixed the width of the conduit to 30 m, a value obtained from geochemical and magma flux observations (Sparks *et al.* 2000). The conduit length ranges 600–1000 m. The upper value may be too large in reality, but it
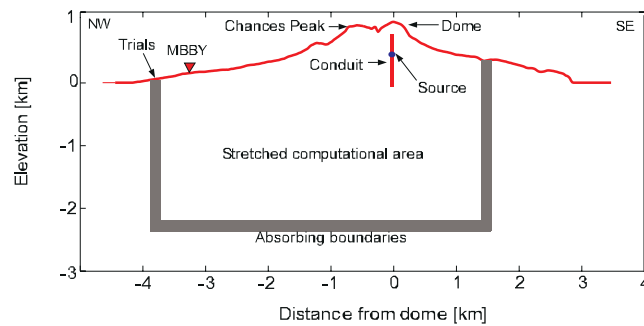
Figure 6. Model used in our finite-difference scheme.

allows us to highlight features of the synthetic low-frequency earthquake more clearly. The depth of the top of the conduit is set to 100 m, except for one case, where this depth is 1000 m. In geological terms, a volcanic conduit always reaches the surface, however, for modelling purpose of seismic signals in a fluid phase, the top end of the our conduit represents the boundary between fluid magma with low-viscosity and high-viscosity magma, which is degassed and almost fully crystallized. The bottom of the conduit represents the level above which bubbles nucleate, providing a strong impedance contrast (Jousset *et al.* 2003; Sturton & Neuberg 2003). We apply realistic velocities for the solid ($V_P = 3000$ m s^{-1}, $V_S = 1732$ m s^{-1}), and a density of $\rho = 2500$ kg m^{-3}. The values of the magma velocity and density are assumed to be constant and uniform as $V_P = 1000$ m s^{-1} and $\rho = 2270$ kg m^{-3}, respectively. Attenuation is quantified using the quality factor as described in the previous sections and ranges from $[20 < Q < \infty]$ in the solid and from $[5 < Q < \infty]$ inside the magma.

The computational domain extends 3000 m vertically and 10 000 m horizontally. The grid spacing is 2 m ensuring a numerical dispersion of less than 2 per cent, for all frequencies of the source function (Fig. 4). This function is applied inside the conduit at a depth of 450 m below the surface. We start with a flat stress-free surface and later introduce topography simulating active dome of Soufrière Hills volcano, Montserrat. In order to represent the topographic model we use a 2-D cubic B-spline interpolator with a sampling interval of 30 m to extract a NW–SE profile from a 3-D digital elevation model. In our example, we used a 3-D digital elevation model of Montserrat with a resolution of 10 m. This smoothing operation allows us to avoid spatial aliasing from high-wavenumber topographic features. The profile is then resampled with a 1-D cubic B-spline interpolator according to the much higher resolution of the finite-difference grid spacing and introduced as the topography function z_0 in eqs (17) and (18). Absorbing boundary conditions are defined at the sides of the grid using a paraxial approximation of the elastic wave equation at the boundary (Clayton & Engquist 1977), an exponential damping zone (Cerjan *et al.* 1985) and a linear decrease of the quality factor from its value in the medium to $Q = 2$ at the boundary (Hestholm 1999).

To investigate the effect of attenuation and topography on waveforms, amplitudes spectra and dispersion, we compute the wave propagation in a series of models, of increasing complexity. We first describe fundamental characteristics of low-frequency seismograms in Section 4.2. In Section 4.3, we investigate the effect of Q ($Q = 5, 10, 20, 100$) in the conduit of fixed length (1000 m) and the effect of conduit length for $Q = 10$, with elastic surrounding medium, and where there is no topography. We demonstrate that conduit resonance is possible if Q is high enough for a given conduit length and if the conduit is long enough for a given Q. We investigate the dispersion within the coda of the signal in Section 4.4. Finally, in Section 4.5, we illustrate scattering of low-frequency earthquakes as a result of topography and we vary the position of the conduit at depth. Seismograms, spectra and spectrograms are shown for positions at the free surface at 100 m or/and 1500 m from the conduit.

4.2 Fundamental characteristics of low-frequency seismograms

Regardless of the model parameters we use, the synthetic low-frequency seismograms recorded at the free-surface display fundamental characteristics, similar to those observed in data: the duration of the synthetic seismograms last several seconds and the spectra displays harmonic low-frequency peaks. The nature of these low-frequency synthetic earthquake is described in Aki *et al.* (1977); Chouet (1985, 1986, 1988, 1992, 1996b); Neuberg (2000). A detailed description can be found in Jousset *et al.* (2003). After the source has been excited within the conduit, seismic energy propagates as *P* waves, converted *S* waves and interface waves at the boundaries of the conduit (Fig. 7). The body waves propagate through the medium to the stations and allow us to locate the source location of these events, by using conventional traveltime techniques. The interface waves propagate up and down the conduit and cause the conduit resonance. Depending on the choice of parameters, two interface wave types are observed: one travels faster than the acoustic velocity in the conduit and has normal dispersion; the other has a slower speed than the accoustic velocity and shows inverse dispersion. These interface waves display elliptical, retrograde particle motions and their amplitudes decay exponentially with the distance from the conduit. Seismic energy is released at the ends of the conduit as *P* and *S* waves. At the top end of the conduit, the energy is converted at the free surface and propagates along it, with characteristics of Rayleigh waves. The synthetic seismogram of a low-frequency event is hence a superposition of all these forms of seismic energy (Fig. 7).

The numerical computations show that the slow, inverse dispersive interface waves have the largest amplitudes. As they propagate along the conduit, seismic amplitudes and frequencies are governed by the physical properties within the conduit and the media. The coda of the signal comprises single wavelets corresponding to interface waves that have been reflected several times at the conduit ends. Therefore,
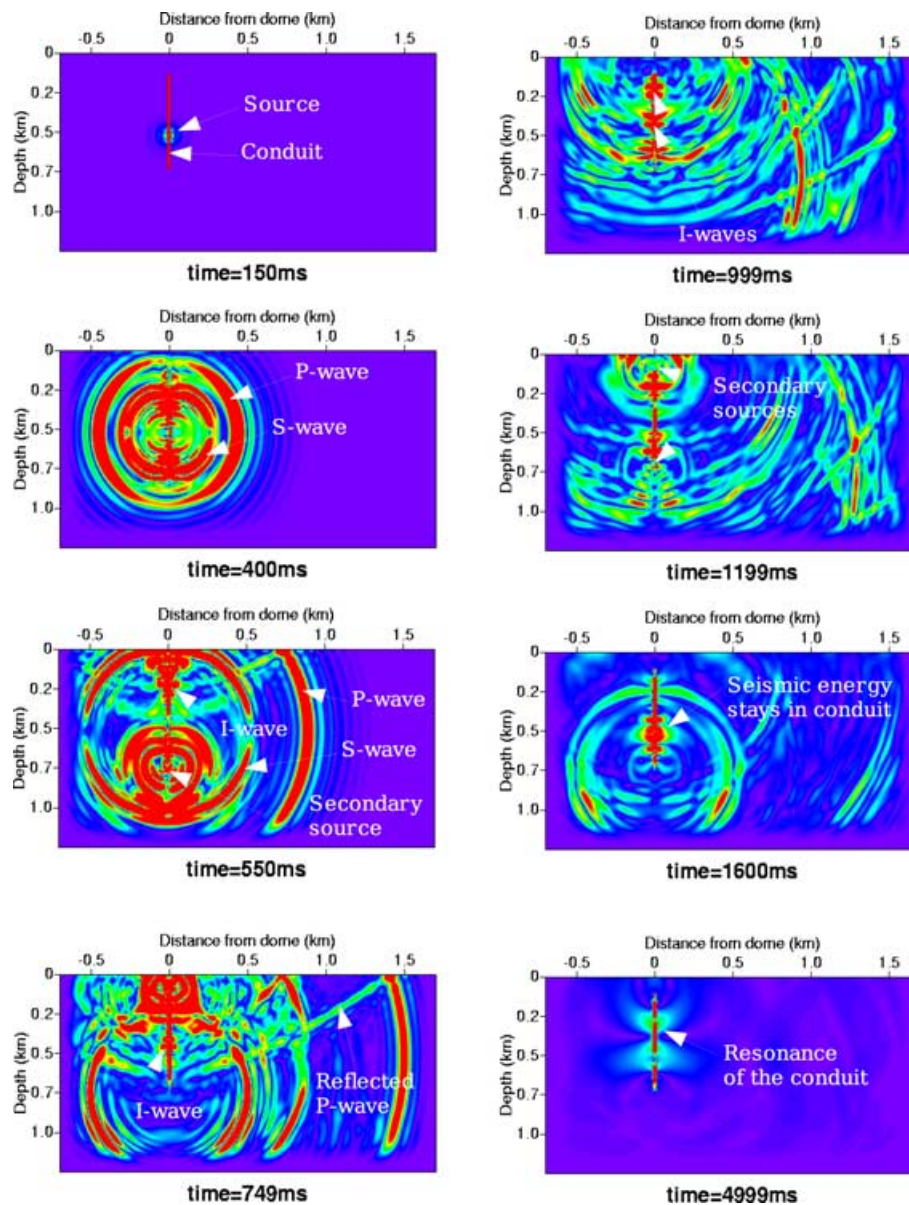
Figure 7. Series of snapshots of the amplitude of the velocity wavefield. The conduit is 600 m long and 30 m wide. The density of the solid is 2500 kg m^{-3} and the density of the conduit is 2270 kg m^{-3}. Elastic velocities are $V_P = 1000$ m s^{-1} in the conduit, and $V_P = 3000$ m s^{-1} and $V_S = 1732$ m s^{-1} in the medium. Quality factors in the solid are $Q_P = 200$ and $Q_S = 100$, and in the conduit $Q = 50$. The quality factor and the phase velocity are shown in Fig. 5.

analysis of waveforms, particle motions, spectra and dispersive characteristics of low-frequency earthquakes can give insights into magma properties and geometry of the conduit. As later wavelets spend more time in the conduit than earlier phases, (i) amplitudes of successive wavelets decay according to a simple rule, which we derive in Section 4.3, and (ii) dispersion increases within the coda of the signal, as shown in Section 4.4.

4.3 Amplitude decay

The amplitude of seismic waves decays as a result of geometrical spreading, internal friction, which converts seismic energy into heat (intrinsic attenuation), and scattering. The amplitude decay observed from seismic signals has been used to locate pyroclastic flows (Jolly *et al.* 2002), volcanic earthquakes (Battaglia *et al.* 2003) and tremor (Gottschammer & Surono 2000). Alternatively, the amplitude decay within long-period seismograms has been used to determine an apparent attenuation (Kumagai & Chouet 1999, 2000a,b; Kumagai *et al.* 2002a; Seidl & Hellweg 2003).

In order to understand how the amplitudes decay in our synthetic seismograms as the result of geometrical spreading and attenuation in the conduit, we measure peak-to-peak amplitudes of the successive wavelets in the coda, for various values of Q in the conduit (length 1000 m), the surrounding medium being elastic (Figs 8 and 9). We compare these synthetic amplitudes with theoretical amplitudes, obtained using amplitude decay resulting from 2-D geometrical spreading, reflection and transmission at the top and the bottom of the conduit, and
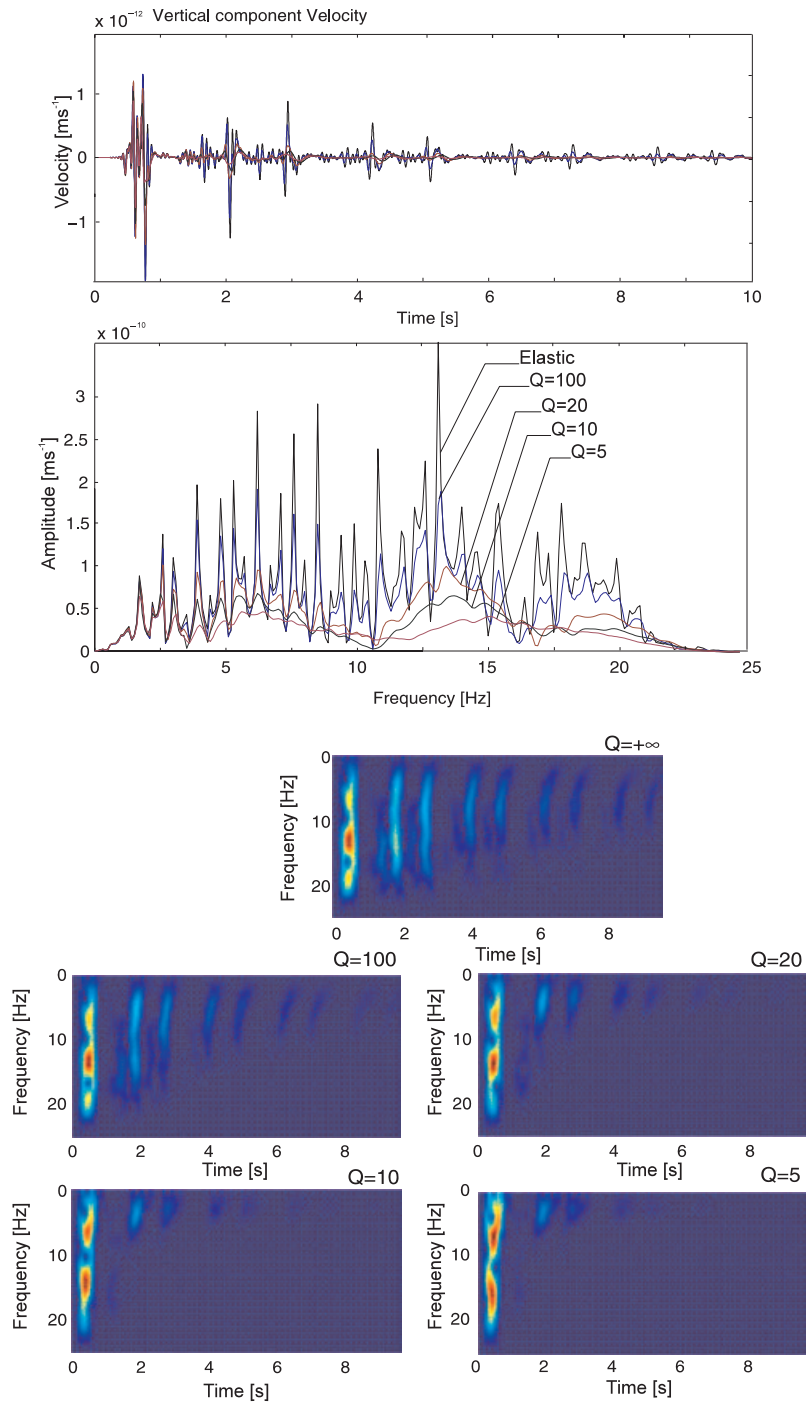
Figure 8. Seismograms (vertical component of the velocity), spectra, spectrograms, recorded at a virtual seismometer located at the free-surface at 100 m from the conduit, using a broad-band (0–25 Hz) source, in various anelastic media, ($Q = +\infty$, $Q = 100, 20, 10, 5$) with one relaxation mechanism for modelling a constant Q between 2 and 25 Hz. The quality factors are $Q_P = Q_S = +\infty$ in the medium outside the conduit. In the solid, P-wave velocity is $V_P = 3000$ m s^{-1}, S-wave velocity is $V_P = 1732$ m s^{-1}, the density is $\rho = 2500$ kg m^{-3}. In the conduit (30 m wide, 1000 m long), $V_P = 1000$ m s^{-1}, $\rho = 2270$ kg m^{-3}. In the seismograms, there are five superimposed seismograms, corresponding to the five Q values. Both in seismograms and spectra, the lower the Q, the lower the amplitude. In the spectrograms, the local spectra are computed using a 0.5-s window.

intrinsic attenuation of waves travelling in the conduit. As we have 2-D seismograms, interface waves propagate along the conduit without loosing energy. The impedance contrast between conduit and surrounding medium defines the reflection coefficient of a seismic wave with vertical incidence as (Ben-Menahem & Singh 2000)

$$R = \frac{\rho_l V_{I_l} - \rho_m V_{p_m}}{\rho_l V_{I_l} + \rho_m V_{p_m}} \tag{41}$$

© 2004 RAS, *GJI*, **159,** 776–802
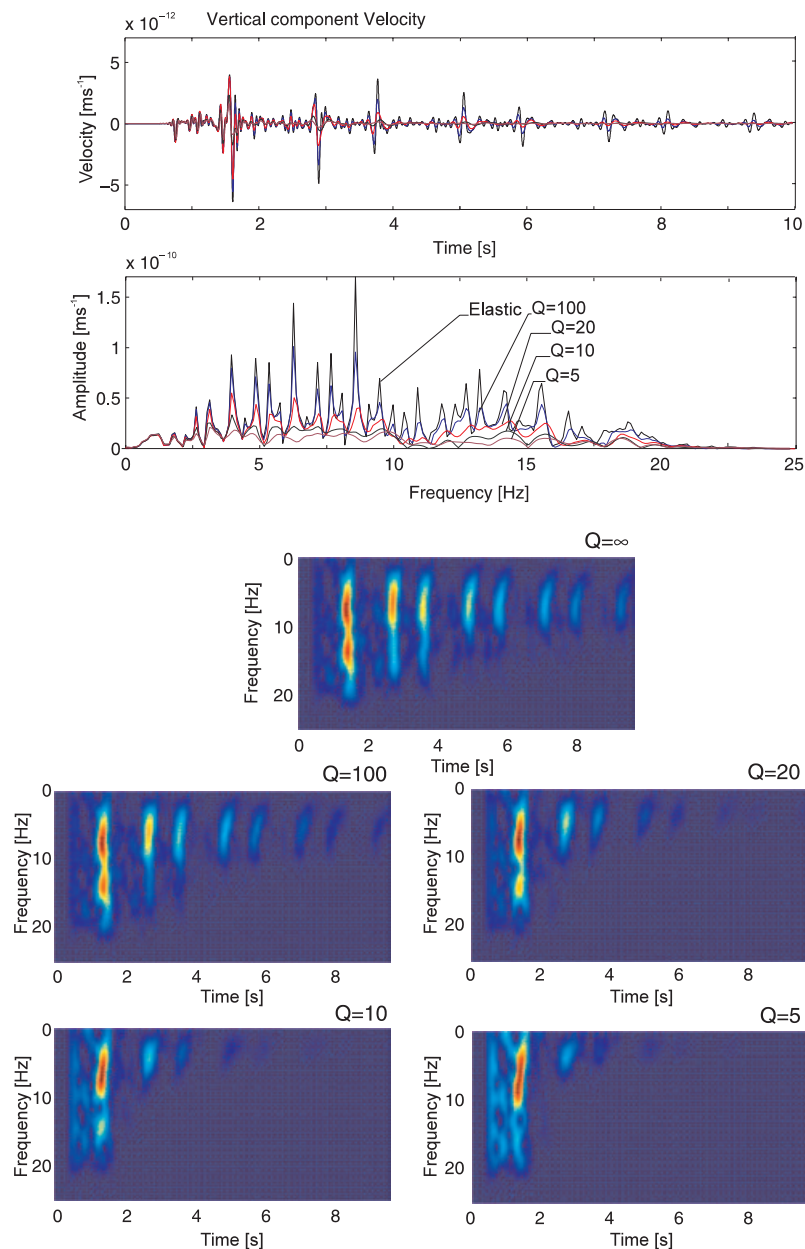
Figure 9. Same as Fig. 8 for a seismometer located at 1500 m from the conduit.

and the amplitude reflection coefficient $T = 1 - R$, where ρ_l and ρ_m are the densities of the fluid and the solid, respectively, and V_{I_l} is the interface wave velocity and V_{P_m} is the acoustic velocity in the solid.

Fig. 10 reveals that synthetic and theoretical amplitudes diverge, the synthetic amplitudes getting larger than the theoretical amplitudes, with distance/time. This is explained by using a frequency-independent Q. Starting with a broad frequency spectrum (0 to 20 Hz), attenuation modelled with a constant Q makes amplitudes of the higher frequencies (>10 Hz) decay faster than the amplitudes of the lower frequencies. Accordingly, the peak-to-peak amplitudes are sampled at all frequencies in the earlier wavelets, compared with the amplitudes sampled at low frequencies for later wavelets.

Amplitudes of the synthetic seismograms and theoretical amplitudes match however reasonably well (Fig. 10). This result demonstrates that the coda of the low-frequency earthquake cannot be directly linked to the attenuation in the conduit only. The apparent quality factor obtained from the coda of low-frequency earthquakes (Seidl & Hellweg 2003) is smaller than the actual wave attenuation in the conduit. By neglecting energy leakage at the conduit ends, the amplitude decay is solely attributed to intrinsic attenuation in magma and therefore this effect is overestimated. For a purely elastic wave, the amplitude decay is only a result of energy leakage. By assuming conduit geometry and magma properties (velocity and density), an estimation of the true quality factor can be then obtained interpreting the coda decay of observed low-frequency seismograms, as a superposition of single, damped, reflected wavelets.
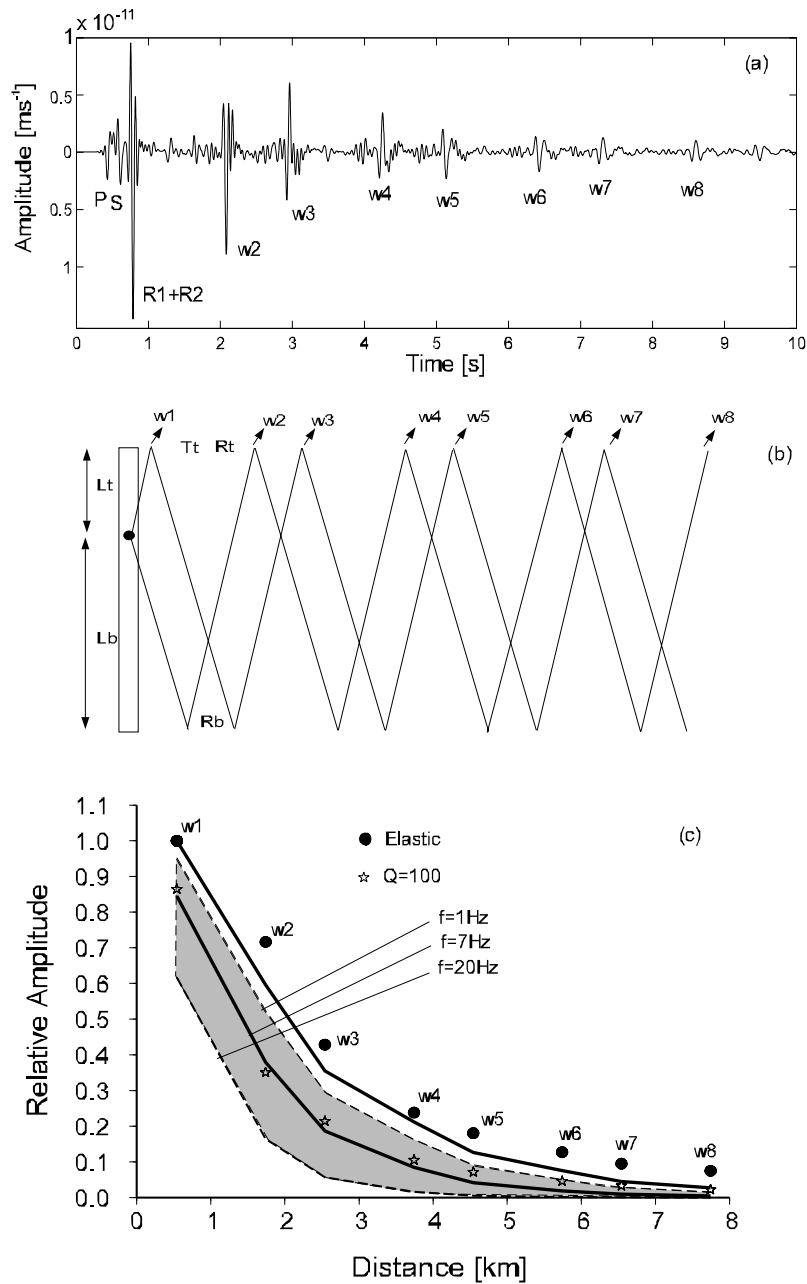
Figure 10. (a) Seismogram (vertical component) recorded at a seismometer at the free surface at 100 m from the conduit. Letters indicate phases, i.e. *P* stands for *P*-wave, *S* for *S*-wave, w_i for the *i*th wavelet emitted at the conduit top end. Pairs of wavelets may be classified according to their first motion polarity. Couples $\{w_1, w_2\}$ and $\{w_5, w_6\}$ have an upward first motion, while pairs $\{w_3, w_4\}$ and $\{w_7, w_8\}$ have a downward first motion. The first motion polarity for each wavelet pair corresponds to the number of reflections of the initial energy pulse at the conduit bottom end. (b) Schematic building of a synthetic volcanic low frequency, by addition of successive wavelets, from the top and the bottom of the conduit, acting as secondary sources. The amplitude of each wavelet in the signal is determined by the impedance contrast between the fluid-filled conduit and the solid surrounding medium. (c) Relative peak-to-peak amplitude of successive wavelets in the coda: black dots, elastic case; stars, anelastic case ($Q = 100$ in the conduit). Amplitude decays according to the rate of the theoretical seismic energy leakage (top continuous black line), computed using eq. (41). In the anelastic case, amplitude decays faster according to intrinsic attenuation. The bottom black line corresponds to a signal of frequency of 7 Hz; the grey area indicates the range of amplitude decay according to the wavelet frequency (2 to 20 Hz).

Viscoelastic synthetics presented up to here display a clear sequence of phases separated by intervals of low-amplitude signals, because the conduit is long enough and because the frequency content of the source is up to 20 Hz. When the frequency content of the source is lower and/or when the conduit is shorter, identification of phases is less straightforward, because successive wavelets are interfering one with another. Fig. 11 demonstrates also that a too small conduit section does not allow resonance to carry on for a long time. This suggests that the use of such wavelets in data could allow us to derive the geometry of the conduit from the delay between them and separate them from magma properties in the conduit.
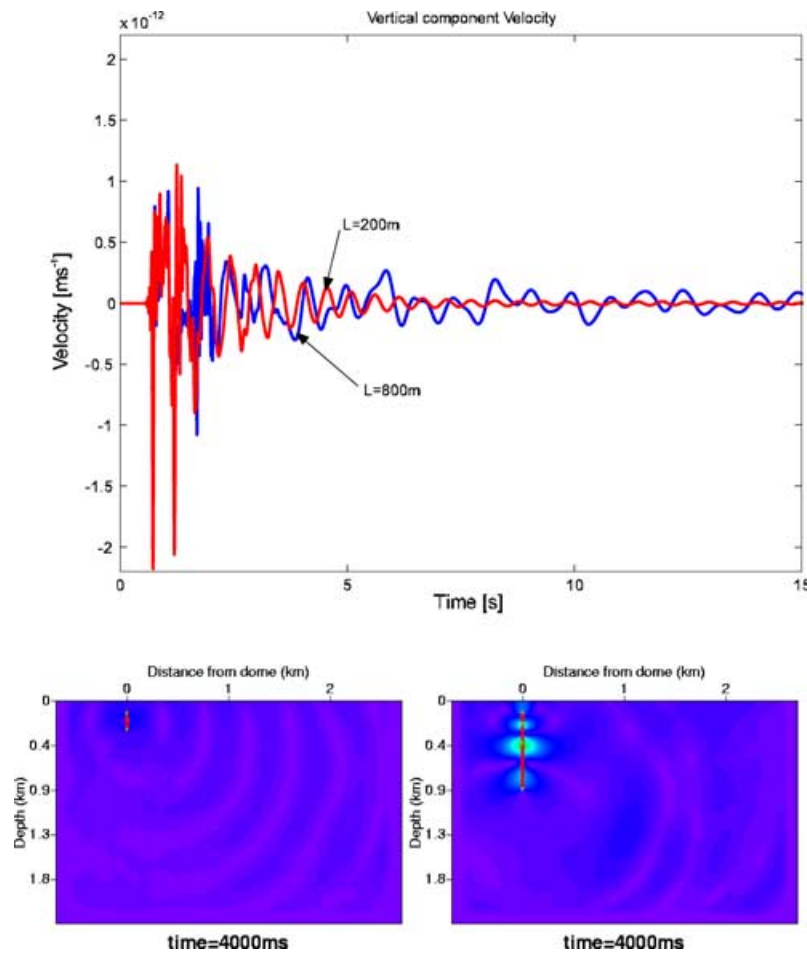
Figure 11. (top) Superposed seismograms recorded at a seismometer located at 1500 m from the conduit. The fluid velocity is $V_P = 1000$ m s^{-1} and $Q = 10$ in the conduit. The surrounding media is elastic. (bottom) Two snapshots taken at a time 4 s, showing that resonance in (right) longer conduit sections (length 800 m) lasts for a longer time than (left) in shorter conduit sections (length 200 m).

4.4 Dispersion analysis

Low-frequency waveforms are by nature dispersive, when they are produced in a crack system (Chouet 1986; Ferrazzini & Aki 1987). In our model, as interface waves propagate further along the conduit, normal and inverse dispersion are observed (Jousset *et al.* 2003). Slow wavelets display more dispersion than the fast ones, because of their longer journey in the conduit (Figs 8 and 9).

   If attenuation is introduced, dispersion increases. Figs 12 and 13 illustrate the effect that Q has on dispersion, regarding waveforms and normalized particle motions. In the seismograms, the single wavelets stretch apart and the seismic energy is distributed over a longer time. This demonstrates that, the lower Q is, the more dispersion occurs. In addition, in the elastic case, the successive wave packets display an alternative polarity, which is in direct relation to the polarity at the source and the number of reflections/transmission at the top of the conduit (Fig. 10). When attenuation is introduced, the particle motions of successive wavelets are affected (Fig. 13). This alternating pattern is destroyed when attenuation is very strong (e.g. see case $Q = 10$ in the conduit). It is also possible to discriminate between cases in which Q is set inside or outside the conduit (Fig. 12). When attenuation changes in the conduit (Fig. 12b), the frequency content is stretched, resulting in a wider frequency spectrum and each spectral peak is broadened. On the other hand, when attenuation changes in the outside medium (Fig. 12c), all frequencies are shifted, but neither the frequency interval between the peaks, the relative amplitude between the peaks, nor the sharpness of the peaks are altered. This allows the identification of the main source of attenuation.

   In observed seismograms, depending on the station location, some waveforms (e.g. Fig. 1) exhibit phases of larger amplitude, which could correspond to the successive wavelets released at the top of the conduit. However, it is difficult to recognize such patterns in data and identify clearly successive wavelets, dispersion and polarization patterns, because these characteristics are altered by the topography and the *P*- and *S*-wave velocity structures.

4.5 Effect of the topography

Topography is known to affect the particle motion and waveform depending on the relationship between seismic frequency and topographic wavelength (Ohminato & Chouet 1997; Neuberg & Pointer 2000; Regnier *et al.* 2000; Zaslavsky & Shapira 2000). Several studies demonstrated
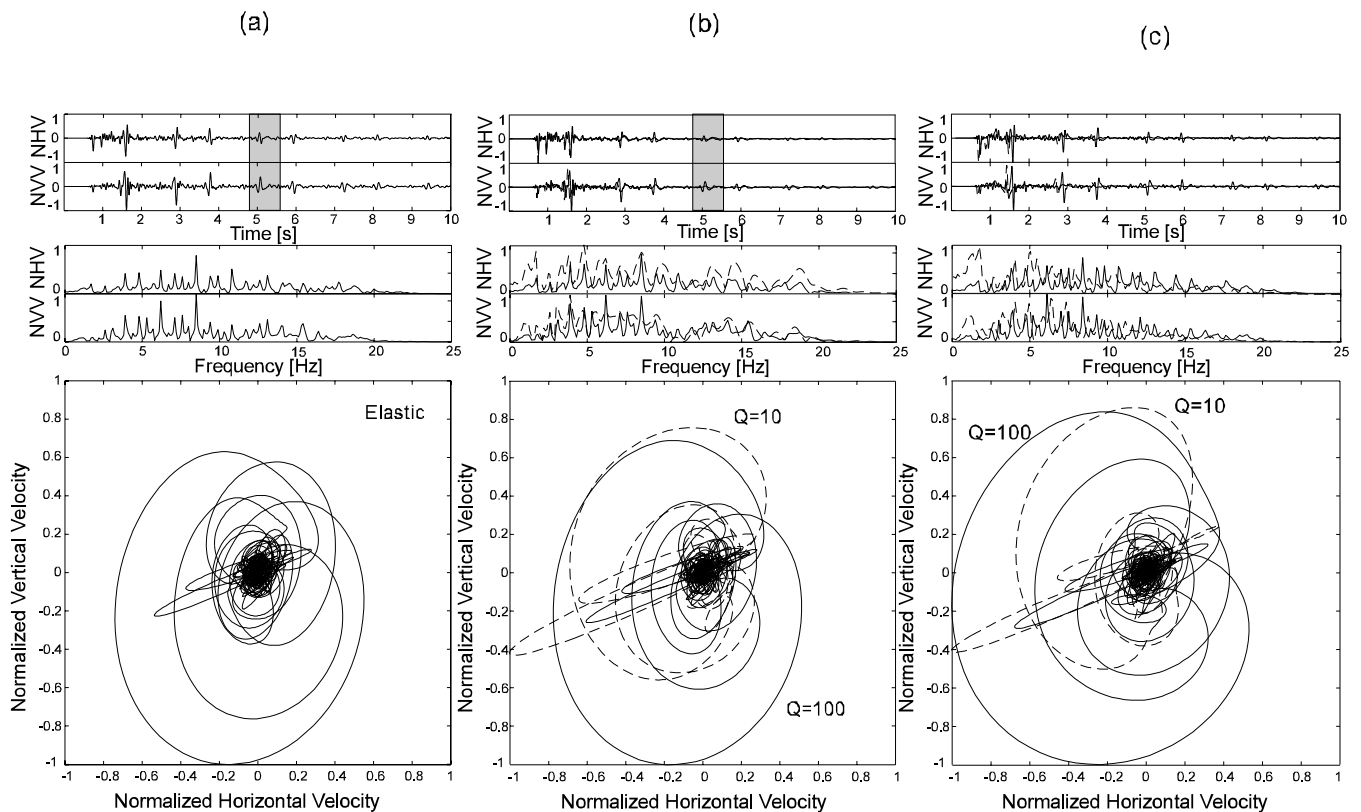
Figure 12. Seismograms, spectra and particle motions of records at a seismometer located at 1500 m from the conduit. (a) Both conduit and surrounding medium are elastic; (b) the conduit only is anelastic with $Q = 100$ (plain line) and $Q = 10$ (dashed line); (c) the medium only is anelastic with $Q = 100$ (plain line) and $Q = 10$ (dashed line). NVV and NHV stand for normalized vertical velocity and normalized horizontal velocity, respectively. The grey area in the seismograms corresponds to the detailed wavelet in Fig. 13.

the topographic scattering effects for simple point sources. Volcanic low-frequency seismic events are particularly strongly affected by topography, as a result of (i) the ruggedness of topographic features on volcanoes and (ii) the shallow position of the upper conduit end that acts as the secondary source from which low-frequency events are radiated. In order to illustrate the combined effects of conduit resonance and topography, we compute several examples using cross-sections of Montserrat topography (Fig. 14). Our Montserrat topography profiles feature the active dome and we show the profile in which the seismic station MBGA is located at a distance of 1500 m from the dome.

In Fig. 15, we investigate the influence of topography and source model and source position by comparing four different cases: (i) point source at 600 m and topography, (ii) anelastic conduit model (at 100 m depth) without topography (model used so far with $Q = 100$ in the medium), (iii) conduit at 1000 m and topography, (iv) conduit at 100 m and topography.

In all cases, topographic scattering of seismic waves results in more complex waveforms. To compare cases (i) and (iv), Fig. 16 shows snapshots of the velocity field amplitude for a point and conduit source, respectively, illustrating the complex topography scattering on seismic signals. The complex wavefield resulting from conduit resonance shows additional wavelets of scattered seismic energy, which also alters the amplitude spectrum. This demonstrates that an interpretation of spectral peaks in terms of source resonators is rather questionable (Seidl & Hellweg 2003). However, time-dependent spectral features nevertheless reflect changes in volcanic source processes (Neuberg & O'Gorman 2002; Jousset *et al.* 2003).

To compare (ii) and (iv), we depict resulting waveforms, spectra and particle motions in Fig. 17 for successive wavelets. The originally elliptical particle motion as well as the amplitudes are highly affected by topography if the dominant topographic wavelength matches the Fresnel zone of the seismic signal at the free surface (Neuberg & Pointer 2000).

5 CONCLUSIONS AND DISCUSSION

Low-frequency volcanic earthquakes characteristics are dependent on the conduit geometry and physical properties of magma (Neuberg *et al.* 1998; Neuberg 2000; Jousset *et al.* 2003; Sturton & Neuberg 2003). By fixing the geometry of the conduit, we investigated effects of attenuation and topography on amplitudes and waveforms of synthetic low-frequency seismograms using 2-D finite-difference modelling of viscoelastic wave propagation in a simplified volcanic structure bounded by a realistic topography. For many tested models, the fundamental
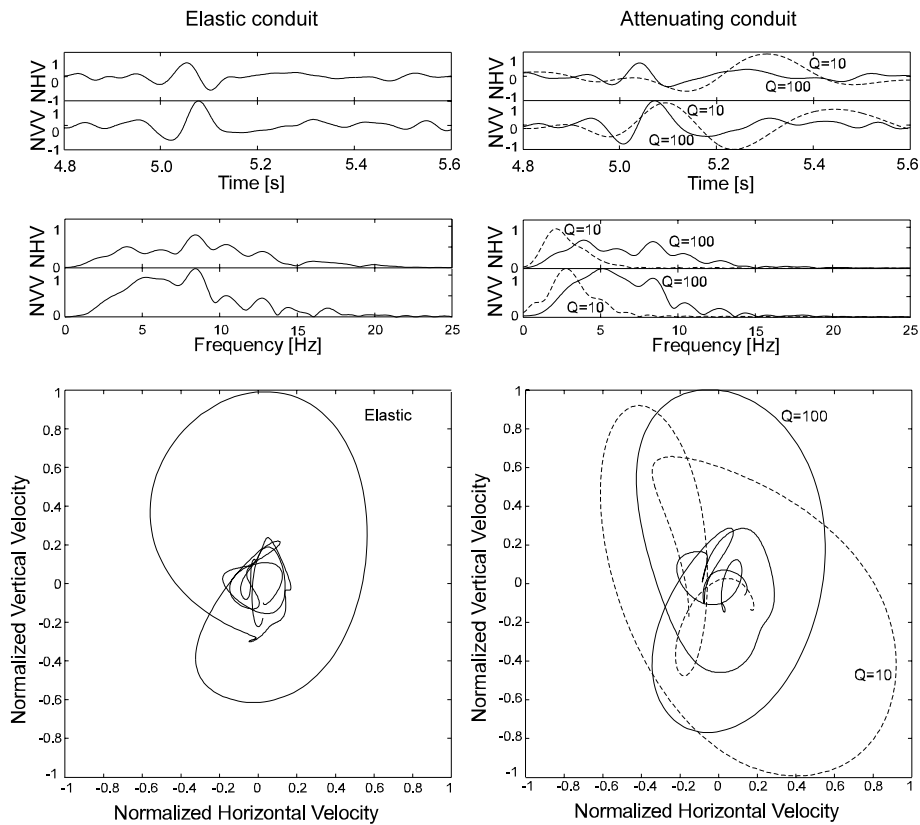
Figure 13. Detailed waveform analysis of the wavelet w_4 (Fig. 10) extracted from the vertical component of the seismogram shown in Fig. 12. (left) Elastic medium and conduit. (right) Elastic medium and anelastic conduit. Attenuation stretches wavelets and modifies waveforms and particle motions.
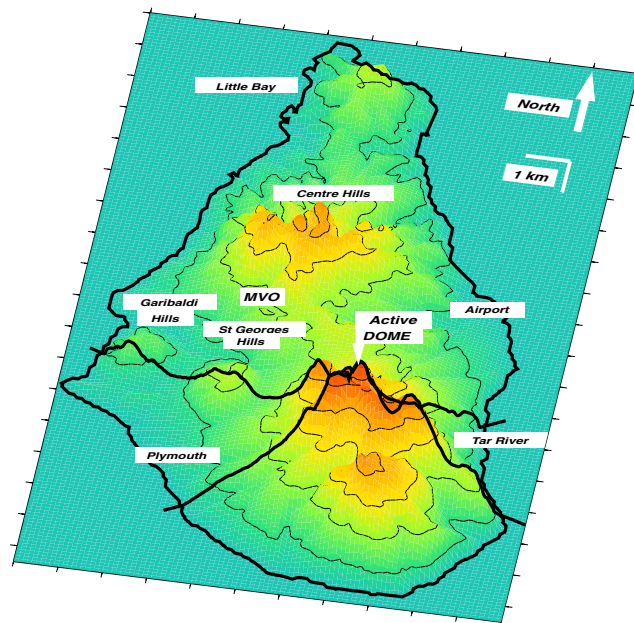
Figure 14. 3-D topographical map of Montserrat island, revealing the steep slopes of the volcano. The view is taken from the azimuth 170° from N with an vertical view angle of 45°. The black lines across the island indicate two topography profiles used to compute our synthetics.

characteristics of observed volcanic low-frequency earthquakes are reproduced. We confirm that conduit sections act as resonators, where the top and bottom ends provide seismic reflectors and therefore secondary seismic sources. In this study, we addressed four questions.

(i) We investigated the effect of anelasticity on characteristics of the frequency content and dispersion of low-frequency earthquakes. The 2-D conduit model explains most of the characteristics of low-frequency earthquake. Attenuation reduces amplitudes and enhances the
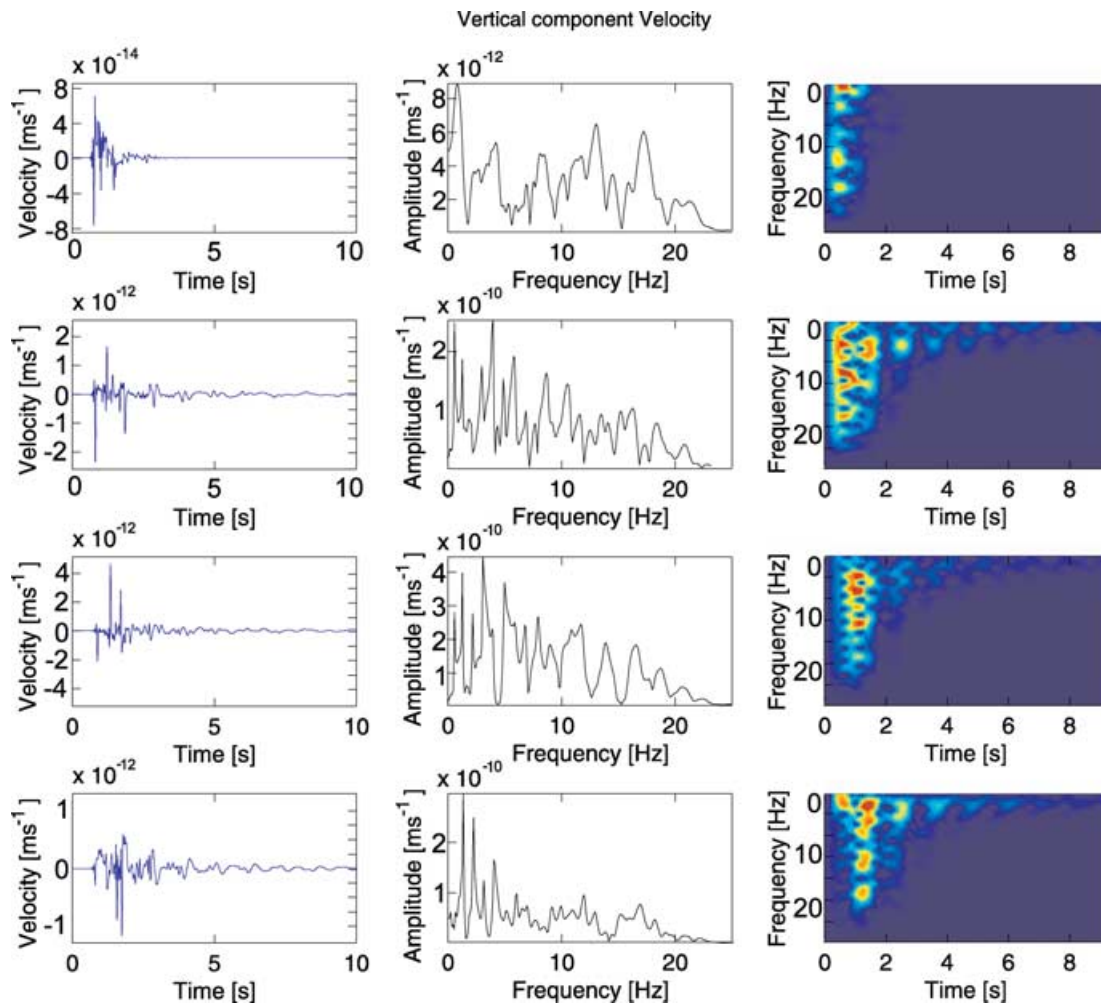
Figure 15. Seismogram, amplitude spectra and spectrograms recorded on vertical component of a seismometer located on the free surface (NW–SE profile of Montserrat topography, except for b), at a distance of 1500 m from the source (R1500 in Fig. 16). (a) there is no conduit; (b) the conduit is present (conduit length 1000 m) and the free surface is flat (no topography); (c) the top of the conduit is 1000 m depth; (d) the top of the conduit is 100 m depth. The density of the solid is 2500 kg m^{-3}. Elastic velocities are $V_P = 3000$ m s^{-1} and $V_S = 1732$ m s^{-1} in the medium. In the conduit, $V_P = 1000$ m s^{-1} and the density is 2270 kg m^{-3}. The quality factors in the solid are $Q_P = 150$ and $Q_S = 100$. When the conduit is present, $Q = 20$ in the conduit. Attenuation is computed using three relaxation mechanisms.

intrinsic dispersion of the low-frequency signal. We showed that the conduit acts as a resonator provided attenuation in the conduit is not too low, $Q > 10$. Based on qualitative resemblance between seismograms, spectra and spectrograms, we suggest that attenuation in the conduit at Montserrat is rather weak.

(ii) We studied the impact of topography on waveform and amplitude of low-frequency earthquakes. Topography modifies traveltimes and waveforms of low-frequency earthquakes. This makes it difficult to identify models that would produce waveforms matching the observations. For volcanoes with steep topography, the frequency content of low-frequency events is a superposition of conduit resonance and topography scattering. Therefore, single frequency peaks cannot be interpreted as source processes.

(iii) We suggested a strategy to estimate attenuation within volcanic media, by separating and interpreting single wavelets in low-frequency volcanic earthquakes as repeatedly reflected, damped energy packages. The analysis of the amplitude decay in the coda allows us only to get an apparent quality factor, which is lower than the actual intrinsic Q in the magma. This strategy may be difficult to implement in practice as individual wavelets are not commonly identifiable in the decaying code of typical low-frequency events.

(iv) We provided constraints on the rheology of volcanic media on the basis of viscoelastic wave propagation. Using experimental results, we showed that volcanic media may be represented by the SLS at seismic frequencies above 2 Hz. Our results match with observations of seismograms and suggest that the quality factor Q in volcanic media at Montserrat may be between 10 and 100, in accordance with results from other studies, e.g. Jolly *et al.* (2002) and Vanorio *et al.* (2002).

Our study has several limitations. We model attenuation using the SLS, with several relaxation mechanisms. Each relaxation mechanism could correspond to different timescales of stress relaxation, but as many studies did before, we do not relate them to any physical process. The assumption of an SLS fails below 2 Hz and yet low-frequency earthquakes have frequencies below 2 Hz. Diffusive processes may start to
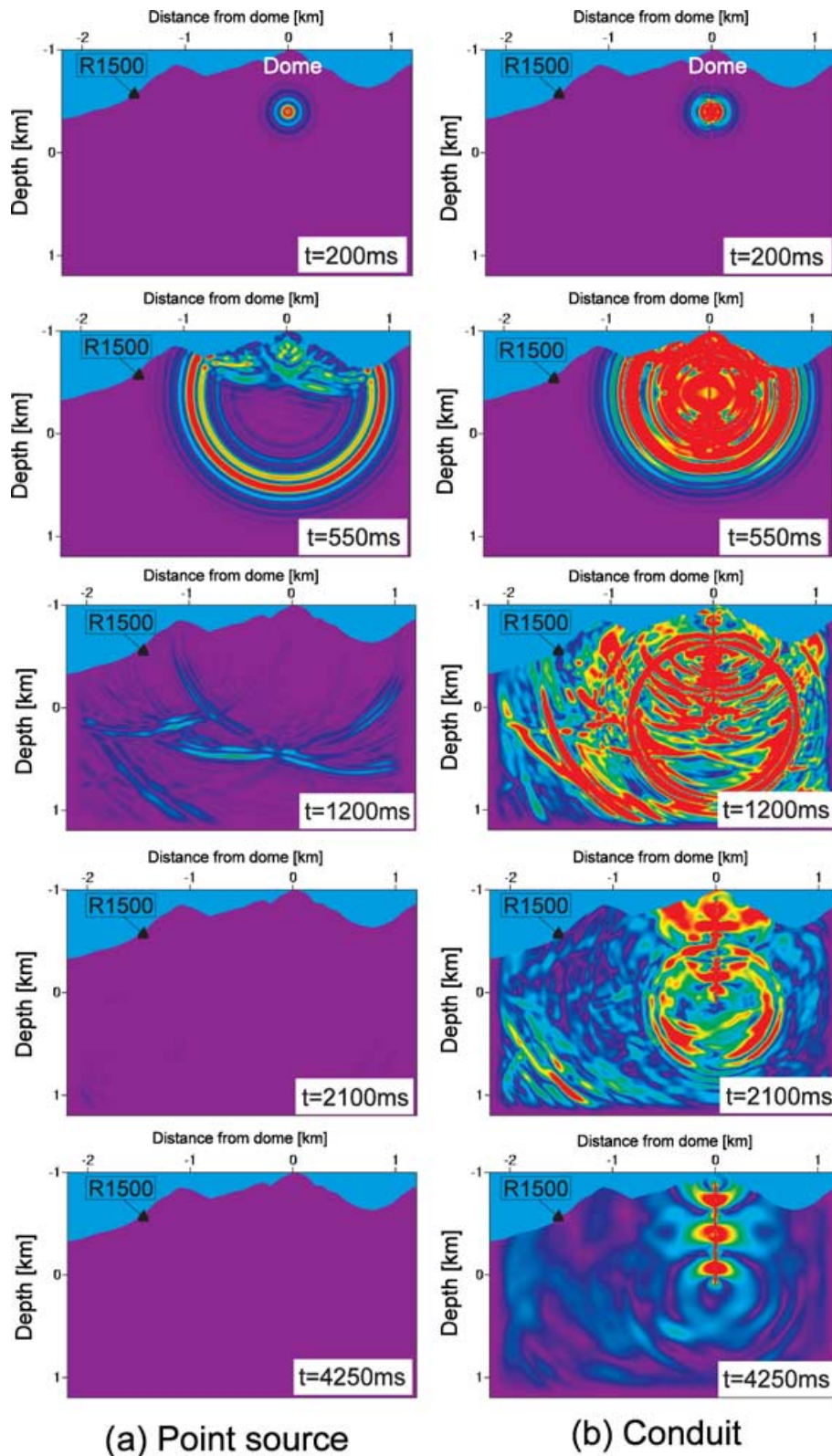
Figure 16. Series of snapshots of the amplitude of the velocity wavefield produced by (a) an explosive point source in the homogeneous medium and (b) the resonance of the conduit ($Q_{\text{conduit}} = 20$). In both examples, the topography crosses the dome along a NW–SE profile. R1500 is the seismometer location for seismograms and particle motions in Figs 15 and 17.
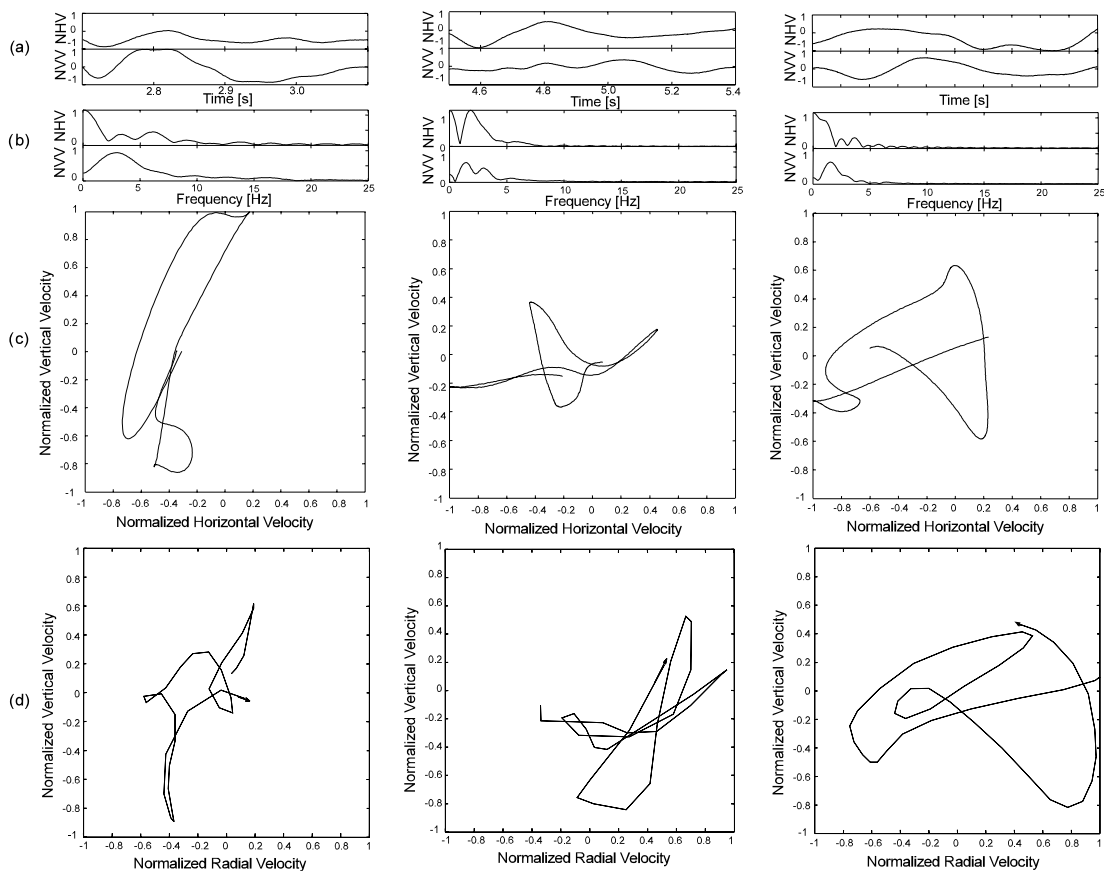
Figure 17. Detailed waveform analysis (0.4 s) of successive wavelets propagating along the surface topography. (a) Horizontal and vertical velocity components recorded at a seismometer located at 1500 m from the dome (see R1500 in Fig. 16); (b) corresponding spectra; (c) corresponding particle motion; (d) observed waveforms from 0.4-s windows extracted from the seismogram in Fig. 1(b) (23:15 h UT).

become important, modifying the way energy is balanced. We considered in this work intrinsic attenuation, but we showed that scattering as a result of the topography and scattering of energy at the ends of the conduit section plays a role as well in the dissipation of seismic energy. Moreover, 3-D effects of the topography are not taken into account into our modelling and they may be important.

One may also wonder about the general applicability of the model to Montserrat. For a basaltic system, in which magma viscosities are within the 10^4–10^7 Pa s range, resonance of a large part of the volcanic system has been shown (Aki *et al.* 1978). At Montserrat, with a viscosity range of 10^9–10^{14} Pa s (Sparks *et al.* 2000), the important question is identifying conditions for which dissipation of seismic energy prevent sustained resonance of the magma column as a whole. The critical medium is the bubbly liquid, where attenuation is the largest. We employed the bubbly liquid model by Commander & Prosperetti (1989) and found *Q* values between 10 and 100 for realistic sets of parameters for Montserrat. A further discussion of this issue is beyond the scope of this paper and is the subject of a study that includes diffusion processes. Moreover, the whole magma column is not only made of viscous liquid and bubbles, but crystals are also present in the rising magma (Sparks *et al.* 2000). Hence, the further study will take crystals into account. A further important step to test our model would be a comparison with a moment–tensor inversion of low-frequency volcanic earthquakes (Legrand *et al.* 2000; Kumagai *et al.* 2002a,b) on Montserrat. This could give further insights into the source mechanism, geometry and its position and orientation.

REFERENCES

Aki, K., 1980. Attenuation of shear-waves in the lithosphere for frequencies from 0.05 to 25 Hz, *Phys. Earth planet. Int.,* **21,** 50–60.

Aki, K. & Richards, P., 2002. *Quantitative seismology,* 2nd edn, University Science Books, Sausalito, CA.

Aki, K., Fehler, M. & Das, S., 1977. Source mechanism of volcanic tremor: fluid-driven crack models and their application to the Kilauea eruption, *J. Volc. Geotherm. Res.,* **2,** 259–287.

Aki, K., Chouet, B., Fehler, M., Zandt, G., Koyanagi, R., Colp, J. & Hay, R.G., 1978. Seismic properties of a shallow magma reservoir in Kilauea Iki by active and passive experiments, *J. Geophys. Res.,* **83**(B5), 2273–2282.

Almendros, J., Chouet, B., Dawson, P. & Bond, T., 2002. Identifying elements of the plumbing system beneath Kilauea Volcano, Hawaii, from the source locations of very-long-period signals, *Geophys. J. Int.,* **148,** 303–312.

Aspinall, W., Lynch, A.M.L., Latchman, J., Stewart, R., White, R. & Power, J., 1998. Soufrière Hills eruption, Montserrat, 1995–1997: volcanic earthquake locations and fault plane solutions, *Geophys. Res. Lett.,* **25**(18), 3397–3400.

Bagdassarov, N. & Dingwell, D., 1992. A rheological investigation of vesicular rhyolite, *J. Volc. Geotherm. Res.,* **50,** 307–322.

Bagdassarov, N. & Dingwell, D., 1993a. Deformation of foamed rhyolites under internal and external stresses: an experimental investigation, *Bull. Volcanol.,* **55,** 147–154.

Bagdassarov, N. & Dingwell, D., 1993b. Frequency dependent rheology of vesicular rhyolite, *J. geophys. Res.,* **98,** 6477–6487.

Bagdassarov, N. & Dorfman, A., 1998. Viscoelastic behavior of partially molten granites, *Tectonophysics,* **290,** 27–45.

Bagdassarov, N., Dingwell, D. & Webb, S., 1994. Viscoelasticity of crystal- and buble-bearing rhyolite melts, *Phys. Earth planet. Int.,* **83,** 83–99.

Barmin, A., Melnik, O. & Sparks, R., 2002. Periodic behaviour in lava dome eruptions, *Earth planet. Sci. Lett.,* **199,** 173–184.

Barnes, H., Hutton, J. & Walters, K., 1989. *An introduction to Rheology,* Elsevier, Amsterdam.

Battaglia, J., Got, J.-L. & Okubo, P., 2003. Location of long-period events below Kilauea using seismic amplitudes and accurate relative relocation, *J. geophys. Res.,* **108**(B12), 2553, doi:10.1029/2003JB002517.

Ben-Menahem, A. & Singh, S.J., 2000. *Seismic waves and sources,* 2nd edn, Dover Publications Inc., Mineloa, NY.

Biot, M., 1952. Propagation of elastic waves in a cylindrical bore containing a fluid, *J. Appl. Phys.,* **23,** 997–1005.

Blanch, J., Robertsson, J. & Symes, W., 1995. Modelling of a constant Q: methodology and algorithm for an efficient and optimally inexpensive viscoelastic technique, *Geophysics,* **60**(1), 176–184.

Bourbie, T., Coussy, O. & Zinzner, B., 1987. *Accoustic of porous media,* Gulf Publ. Co., Houston, TX.

Burdick, L.J., 1985. Estimation of the frequency dependence of *Q* from *ScP* and *ScS* phases, *Geophys. J. R. astr. Soc.,* **80,** 35–55.

Caputo, M., 1967. Linear models of dissipation whose Q is almost frequency independent—II, *Geophys. J. R. astr. Soc.,* **13,** 529–539.

Caputo, M., 1986. Linear and nonlinear inverse rheologies of rocks, *Tectonophysics,* **122,** 53–71.

Carcione, J.M., 1992. Rayleigh waves in isotropic viscoelastic media, *Geophys. J. Int.,* **108,** 453–464.

Carcione, J.M., 1993. Seismic modeling in viscoelastic media, *Geophysics,* **58,** 110–120.

Carcione, J.M., Kosloff, D. & Kosloff, R., 1988. Viscoacoustic wave propagation simulation in the Earth, *Geophysics,* **53**(6), 769–777.

Carcione, J.M., Herman, G.C. & ten Kroode, A.P.E., 2002. Seismic modelling, *Geophysics,* **67**(4), 1304–1325.

Cerjan, C., Kosloff, D., Kosloff, R. & Reshef, M., 1985. A non-reflecting boundary condition for discrete acoustic and elastic wave equations, *Geophysics,* **50,** 705–708.

Chan, W. & Mitchell, B., 1985. Surface wave dispersion, crustal structure, and sediment thickness variations across the Barents sea, *Geophys. J. R. astr. Soc.,* **80,** 329–344.

Chen, G., 1996. Comparison of 2-D numerical viscoelastic waveform modelling with ultrasonic physical modelling, *Geophysics,* **61,** 862–871.

Chouet, B., 1985. Excitation of a buried magmatic pipe: a seismic source model for volcanic tremor, *J. geophys. Res.,* **90,** 1881–1893.

Chouet, B., 1986. Dynamics of a fluid-driven crack in three dimensions by the finite difference method, *J. geophys. Res.,* **91,** 13 967–13 992.

Chouet, B., 1988. Resonance of a fluid-driven crack: radiation properties and implications for the source of long-period events and volcanic tremor, *J. geophys. Res.,* **93,** 4375–4400.

Chouet, B., 1992. in *Volcano Seismology,* pp. 133–156, eds Gasparini, P., Scarpa, R. & Aki, K., Springer-Verlag, Berlin.

Chouet, B., 1996a. Long-period seismicity: its source and use in eruption forecasting, *Nature,* **380,** 309–316.

Chouet, B., 1996b. New methods and future trends in seismological volcano monitoring, in *Monitoring and Mitigation of Volcano Hazards,* pp. 23–97, eds Scarpa, R. & Tilling, R.I, Springer-Verlag, Berlin.

Chouet, B., Page, R., Stephens, C., Lahr, J. & Power, J., 1994. Precursory swarms of long-period events at Redoubt volcano (1989–1990), Alaska: their origin and use as a forecasting tool, *J. Volc. Geotherm. Res.,* **62,** 95–135.

Christensen, R., 2004. *Theory of viscoelasticity—An introduction,* 2nd Edn, Book News Inc., Portland, OR.

Clayton, R.W. & Engquist, B., 1977. Absorbing boundary conditions for acoustic and elastic wave equations, *Bull. seism. Soc. Am.,* **67**(6), 1529–1540.

Commander, K. & Prosperetti, A., 1989. Linear pressure waves in bubby liquids: comparison between theory and experiments, *J. acoust. Soc. Am.,* **85**(2), 732–746.

Dahlen, F. & Tromp, J., 1998. *Theoretical Global Seismology,* Princeton University Press, Princeton, NJ, p. 1025.

Dingwell, D., 1995. Relaxation in silicate melts: some applications, *Rev. Min.,* **32,** 21–66

Dingwell, D. & Webb, S., 1989. Structural relaxation in silicate melts and non-newtonian melt rheology in geological processes, *Phys. Chem. Mineral.,* **116,** 508–516.

Fehler, M. & Chouet, B., 1982. Operation of a digital seismic network on Mount St. Helens Volcano and observations of long-period seismic events that originate under the volcano, *Geophys. Res. Lett.,* **9,** 1017–1020.

Ferrazzini, V. & Aki, K., 1987. Slow waves trapped in fluid-filled infinite-crack: implication for volcanic tremor, *J. geophys. Res.,* **92**(B9), 9215–9223.

Futterman, W., 1962. Dispersive body waves, *J. geophys. Res.,* **67,** 5279–5291.

Gil Cruz, F. & Chouet, B., 1997. Long-period events, the most characteristic seismicity accompanying the emplacement and extrusion of a lava dome in Galeras Volcano, Colombia, 1991, *J. Volc. Geotherm. Res.,* **77,** 121–158.

Gómez, M. & Torres, C., 1997. Unusual low-frequency volcanic seismic events with slowly decaying coda waves observed at Galeras and other volcanoes, *J. Volc. Geotherm. Res.,* **77,** 173–193.

Gottschammer, E. & Surono, I., 2000. Locating tremor and shock sources recorded at Bromo Volcano, *J. Volc. Geotherm. Res.,* **101,** 199–209.

Gudmundsson, O., Finlayson, D., Itikarai, I., Nishimura, Y. & Johnson, W., 2004. Seismic attenuation at Rabaul volcano, Papua New Guinea, *J. Volc. Geotherm. Res.,* **130,** 77–92.

Hagerty, M., Schwartz, S., Garcés, M. & Protti, M., 2000. Analysis of seismic and accoustic observations at Arenal Volcano, Costa Rica, 1995–1997, *J. Volc. Geotherm. Res.,* **101,** 27–65.

Hellweg, M., 2000. Physical models for the source of Lascar's harmonic tremor, *J. Volc. Geotherm. Res.,* **101,** 183–198.

Hellweg, M., 2003. The polarization of volcanic seismic signals: medium or source?, *J. Volc. Geotherm. Res.,* **128,** 159–176.

Hestholm, S., 1999. Three-dimensional finite-difference viscoelastic wave modelling including surface topography, *Geophys. J. Int.,* **139,** 852–878.

Hestholm, S., 2002. Composite memory variable velocity-stress viscoelastic modelling, *Geophys. J. int.,* **148,** 153–162.

Hestholm, S. & Ruud, B., 2000. 2D finite-difference viscoelastic wave modelling including surface topography, *Geophys. Prospect.,* **48,** 341–373.

Jackson, I. & Paterson, M., 1987. Shear modulus and internal friction of calcite rocks at seismic frequencies: pressure, frequency and grain size dependence, *Phys. Earth planet. Sci.,* **45,** 349–367.

Jackson, I., Paterson, M. & Gerald, J. D.F., 1992. Seismic wave dispersion and attenuation in Aheim dunite: an experimental study, *Geophys. J. Int.,* **108,** 517–534.

Johnson, J. & Lees, J., 2000. Plugs and chugs-seismic and acoustic observations of degassing explosions at Karymsky, Russia and Sangay, Ecuador, *J. Volc. Geotherm. Res.,* **101,** 67–82.

Jolly, A., Thompson, G. & Norton, G., 2002. Locating pyroclastic flows on Soufrière Hills Volcano, Montserrat, West Indies, using amplitude signals from high dynamic range instruments, *J. Volc. Geotherm. Res.,* **118,** 299–317.

Jousset, P., Neuberg, J. & Sturton, S., 2003. Modelling the time-dependent frequency content of low-frequency volcanic earthquakes, *J. Volc. Geotherm. Res.,* **128,** 201–223.

Kampfmann, W. & Berckhemer, H., 1985. High temperature experiments on the elastic and anelastic behavior of magmatic rocks, *Phys. Earth planet. Int.,* **40,** 223–247.

Kubotera, A., 1974. Volcanic tremors at Aso volcano, in *Physical Volcanology,* pp. 29–47, eds Civetta L. *et al.,* Elsevier, Amsterdam.

Kumagai, H. & Chouet, B., 1999. The complex frequencies of long-period seismic events as probes of fluid composition beneath volcanoes, *Geophys. J. Int.,* **138,** F7–F12.

Kumagai, H. & Chouet, B., 2000a. Acoustic properties of a crack containing magmatic or hydrothermal fluids, *J. geophys. Res.,* **105,** 25 493–25 512.

Kumagai, H. & Chouet, B., 2000b. The dependence of acoustic properties of a crack on the mode and geometry, *Geophys. Res. Lett.,* **28,** 3325–3328.

Kumagai, H., Chouet, B. & Nakano, M., 2002a. Temporal evolution of a hydrothermal system in Kuratsu-Shirane Volcano, Japan, inferred from the complex frequencies of long-period events, *J. geophys. Res.,* **107**(B10), 2236.

Kumagai, H., Chouet, B. & Nakano, M., 2002b. Waveform inversion of oscillary signatures in long-period events beneath volcanoes, *J. geophys. Res.,* **107**(B11), 2301.

Legrand, D., Kaneshima, S. & Kawakatsu, H., 2000. Moment tensor analysis of near-field broadband waveforms observed at Aso Volcano, Japan, *J. Volc. Geotherm. Res.,* **101,** 155–169.

Levander, A., 1988. Fourth-order finite-difference P-SV seismograms, *Geophysics* **53,** 1425–1436.

Liu, H. & Anderson, D. & Kanamori, H., 1976. Velocity dispersion due to anelasticity; implications for seismology and mantle composition, *Geophys. J. R. astr. Soc.,* **47,** 41–58.

McDonal, F., Angona, F. & Mills, A., 1958. Attenuation of shear and compressional waves in pierre shale, *Geophysics,* **23,** 421–439.

Madja, G., Chin, R. & Followill, F., 1985. A perturbation theory for Love waves in anelastic media, *Geophys. J. R. astr. Soc.,* **80,** 1–34.

Miller, A. *et al.,* 1998. Seismicity associated with dome growth and collapse at the Soufrière Hills Volcano, Montserrat, *Geophys. Res. Lett.,* **25**(18), 3401–3404.

Neuberg, J., 2000. Characteristics and causes of shallow seismicity in andesite volcanoes, *Phil. Trans. R. Soc. Lond.,* A., **358,** 1533–1546.

Neuberg, J. & O'Gorman, C., 2002. A model of the seismic wavefield in gas-charged magma: application to Soufrière Hills volcano, Montserrat, *Geol. Soc., Lond., Mem.,* **21,** 603–609.

Neuberg, J. & Pointer, T., 2000. Effects of volcano-topography on seismic broadband waveforms, *Geophys. J. Int.,* **143,** 239–248.

Neuberg, J., Baptie, B., Luckett, R. & Stewart, R., 1998. Results from the broad-band seismic network on Montserrat, *Geophys. Res. Lett.,* **25**(19), 3661–3664.

Neuberg, J., Luckett, R., Baptie, B. & Olsen, K., 2000. Models of tremor and low-frequency earthquake swarms on Montserrat, *J. Volc. Geotherm. Res.,* **101,** 83–104.

O'Connell, R.J. & Budiansky, B., 1978. Measures of dissipation in viscoelastic media, *Geophys. Res. Lett.,* **5,** 5.

Ohminato, T. & Chouet, B., 1997. A free-surface boundary condition for incluing 3D topography in the finite-difference method, *Bull. seism. Soc. Am.,* **87**(2), 494–515.

Oldroyd, J., 1964. Nonlinear stress, rate of strain relations at finite rates of shear in so called elasto-viscous liquids, pp. 520–529, ed. Abir, D., Pergamon.

Patane, D., Ferrucci, F. & Gresta, S., 1994. Spectral features of microearthquakes in volcanic areas: attenuation in the crust and amplitude response of the site at Mount Etna, Italy, *Bull. seism. Soc. Am.,* **84,** 1842–1860.

Pipkin, A., 1986. *Lectures on viscoelasticity theory,* Springer Verlag, New York.

Power, J.A. *et al.,* 1994. Seismic evolution of the 1989–1990 eruption sequence of Redoubt Volcano, Alaska, *J. Volc. Geotherm. Res.,* **62,** 69–94.

Ranalli, G., 1995. *Rheology of the Earth,* 2nd edn, Chapman & Hall, London.

Regnier, M., Morris, S., Shapira, A. & Malitzky, A., 2000. Microzonation of the expected seismic site effects across Port Vila, Vanuatu, *J. Earthquake Engineering,* **4**(2), 215–231.

Reiner, M., 1945. A mathematical theory of dilatancy, *Am. J. Math.,* **67,** 350–362.

Ricker, N., 1953. The forms and laws of propagation seismic wavelets, *Geophysics,* **1,** 10–40.

Robertsson, J., 1996. A numerical free surface condition for elastic/viscoelastic finite-difference modelling in the presence of topography, *Geophysics,* **61**(6), 1921–1934.

Robertsson, J., Blanch, J. & Symes, W., 1994. Viscoelastic finite-difference modelling, *Geophysics,* **59**(9), 1444–1456.

Roscoe, R., 1950. Mechanical models for the representation of viscoelastic properties, *Brit. J. Appl. Phys.,* **1,** 171–173.

Rowe, C., Aster, R., Kyle, P., Dibble, R. & Schlue, J., 2000. Seismic and accoustic observations at Mount Erebus volcano, Ross Island, Antartica, 1994–1998, *J. Volc. Geotherm. Res.,* **101,** 105–128.

Ruud, B. & Hestholm, S., 2001. 2D surface topography boundary conditions in seismic wave modelling, *Geophysics,* **49,** 445–460.

Sato, H. & Maghnani, M.H., 1985. Ultrasonic measurements of V_p and Q_p: relaxation spectrum of complex modulus on basalts melts, *Phys. Earth planet. Int.,* **41,** 18–33.

Sato, H., Sacks, S., Murase, T., uncill, G. & Fukuyuma, H., 1989. Q_p-melting temperature relation in peridotite at high pressure and temperature: attenuation mechanism and implications for the mechanical properties of the upper mantle, *J. geophys. Res.,* **94**(B8), 10 647–10 661.

Scherbaum, F., 1990. Combined inversion of the three-dimensional Q structure and source parameters using microearthquake spectra, *J. geophys. Res.,* **95,** 12 423–12 438.

Seidl, D. & Hellweg, M., 2003. Parametrization of multichromatic signals observed at Galeras Volcano (Colombia), *J. Volc. Geotherm. Res.,* **125**(1–2), 171–189.

Sparks, R., Murphy, M., Lejeune, A., Watts, R., Barclay, J. & Young, S., 2000. Control on the emplacement of the andesite lava dome of the Soufrière Hills volcano, Montserrat by degassing-induced crystallization, *Terra-Nova,* **12**(1), 14–20.

Stevenson, R.J., Dingwell, D., Webb, S. & Bagdassarov, N., 1995. The equivalence of enthalpy and shear stress relaxation in rhyolitic obsidians and quantification of the liquid-glass transition in volcanic processes, *J. Volc. Geotherm. Res.,* **68,** 297–306.

Strick, E., 1967. The determination of Q, dynamic viscosity and transient creep curves from waves propagation measurements, *Geophys. J. R. astr. Soc.,* **13,** 197–218.

Sturton, S. & Neuberg, J., 2003. The effects of a decompression on seismic parameter profiles in a gas-charged magma, *J. Volc. Geotherm. Res.,* **128,** 187–199.

Taylor, M. A.J. & Singh, S.C., 2002. Composition and microstructure of magma bodies from effective medium theory, *Geophys. J. Int.,* **149,** 15–21.

Tessmer, E., Kosloff, D. & Behle, A., 1992. Elastic wave propagation simulation in the presence of surface topography, *Geophys. J. Int.,* **108,** 621–632.

Tonn, R., 1989. Comparison of seven methods for the computation of Q, *Phys. Earth planet. Int.,* **55,** 259–268.

Vanorio, T., Prasad, M., Patella, D. & Nur, A., 2002. Ultrasonic velocity measurements in volcanic rocks: correlation with microtexture, *Geophys. J. Int.,* **149,** 22–36.

Virieux, J., 1986. $P - SV$ wave-propagation in heterogeneous media: velocity-stress finite-difference method, *Geophysics,* **51,** 889–901.

Wegler, U., 2003. Analysis of multiple scattering at Vesuvius volcano Italy, using data of TomoVes active seismic experiment, *J. Volc. Geotherm. Res.,* **128,** 45–63.

White, R., 1992. The accuracy of estimating Q from seismic data, *Geophysics,* **57**(11), 1508–1511.

White, R., Miller, A., Lynch, L. & Power, J., 1998. Observations of hybrid seismic events at Soufrière Hills volcano, Montserrat: July 1995 to September 1996, *Geophys. Res. Lett.,* **25**(19), 3657–3660.

Wittlinger, H., Haessler, H. & Granet, M., 1983. Three-dimensional inversion of Q_p from low magnitude earthquakes analysis, *Ann. Geophys.,* **1,** 427–438.

Wuenschel, P., 1965. Dispersive body waves—An experimental study, *Geophysics,* **30,** 539–551.

Young, S., Sparks, S.J., Aspinall, W.P., Lynch, L.L., Miller, A.D., Robertson, R.E.A. & Shepperd, J., 1998. Overview of the eruption of Soufrière Hills volcano, Montserrat, 18 july 1995 to december 1997, *Geophys. R. Lett.,* **25**(18), 3389–3392.

Zaslavsky, Y. & Shapira, A., 2000. Observation of topographic site effects in Israel, *Isr. J. Earth Sci.,* **49,** 111–125.

Zener, C., 1948. *Elasticity and anelasticity of metals,* The University of Chicago Press, Chicago, IL.

Zollo, A., D'auria, L., Matteis, R.D., Herrero, A., Virieux, J. & Gasparini, P., 2002. Bayesian estimation of 2-D P-velocity models from active seismic arrival time data: imaging of the shallow structure of Mt Vesuvius (southern Italy), *Geophys. J. Int.,* **151**(2), 565–582.

Zucca, J. & Evans, J., 1992. Active high resolution compressional wave attenuation tomography at newberry volcano, central cascade range, *J. geophys. Res.,* **97,** 11 047–11 055.